Letters in Applied NanoBioScience
Open-Access Journal (ISSN: 2284-6808)

Article
Volume 13, Issue 2, 2024, 52
https://doi.org/10.33263/LIANBS132.052

In silico Identification of Natural Chromones against SARS-CoV-2 M^{pro} and Mutated Spike RBDs. Molecular Docking, Dynamics Simulations, and Pharmacokinetic Prediction

Premkumar G [1], Karamveer [2], Toka Swu [1,*], Basant K. Tiwary [2]

[1] Department of Chemistry, Pondicherry University, Puducherry, 605014, India
[2] Department of Bioinformatics, Pondicherry University, Puducherry, 605 014, India
* Correspondance: tokaswu.che@pondiuni.edu.in;

Scopus Author ID 9638122700

Received: 24.02.2023; Accepted: 28.05.2023; Published: 30.06.2024

Abstract: Severe Acute Respiratory Syndrome CoronaVirus-2 (SARS-CoV-2) is the virus behind the deadly disease COVID-19. The present work reports the in-silico analysis of 173 natural chromones against the SARS-CoV-2 Main Protease (M^{pro}) and spike Receptor Binding Domain (RBD) of the wild type and its variants. The docking studies revealed that chromones have good binding energy against the targets. They were found to be better than the recently reported drug molecules such as Nirmatrelvir, Dipyridamole, and inhibitor N3 (for M^{pro}) and ceftazidime, kobophenol A (for spike RBDs). Structure-activity relationships emphasized the significance of hydroxyl groups and chromone rings in the ligand system for better binding. Molecular Dynamics (MD) simulations such as Free Energy Landscape, RMSD, RMSF, Rg, and H-bond analysis revealed a positive outcome. MM-PBSA calculations evaluated the binding free energy of the docked complexes and ensured their stability. The stabilizing and destabilizing residues of the proteins were identified through residue-wise decomposition analysis. The pharmacokinetic properties and drug-likeness of the selected chromones were also analyzed. This study emphasizes that the selected chromones could be considered for in-vitro studies to obtain promising leads for drug discovery against SARS-CoV-2.

Keywords: SARS-CoV-2; Docking; MD Simulations; MM-PBSA; ADMET.

1. Introduction

Coronaviruses are a diverse group of viruses that cause mild to severe respiratory infections in humans. Severe Acute Respiratory Syndrome CoronaVirus-2 (SARS-CoV-2) is one such virus that caused the first pandemic of the 21st century in December 2019. The infectious disease caused by this virus was named 'coronavirus disease 2019' (COVID-19) by the World Health Organization (WHO). It started spreading around the globe rapidly due to the high transmissibility nature of SARS-CoV-2. In addition, the humans infected by this virus develop low levels of neutralizing antibodies, which may lead to prolonged disease. Since the outbreak of the deadly COVID-19 has posed an alarming threat to worldwide public health and life, the WHO declared this disease a global pandemic on 11 March 2020. As of 21 February 2023, there have been around 757 million confirmed cases of COVID-19, including more than 6.8 million deaths around the globe [1].

Further, like any virus, SARS-CoV-2 is capable of undergoing mutations naturally. A new variant called 'Omicron' started spreading in many countries with increased transmissibility, and it was declared a 'variant of concern' by WHO in November 2021 [2]. Researchers predicted that are 3686 mutations probable in the future in the receptor-binding domain of the spike protein with increased infectivity [3]. Subsequently, the periodic emergence of various mutated strains may become a potential threat to humans around the globe. The virus's destructive and panicking consequences strongly emphasize the urgent need for drug discovery against COVID-19.

The numerous drug repurposing and clinical trials for vaccine development show the importance and necessity of the drugs against SARS-CoV-2. In this regard, the research on SARS-CoV-2 inhibition at a molecular level is essential for developing a competent drug. Also, evaluating the lead compounds against the original and mutated strains is indispensable to tackle the immune evasion tendency that may arise in future mutants. Developing drugs that aim at the essential proteins in the viral life cycle will be a rational approach to choosing therapeutic targets [4]. For example, the Receptor Binding Domain (RBD) of the spike protein serves as an essential functional component for the binding of SARS-CoV-2 by ACE2 to enter the target cells [5]. Also, the SARS-CoV-2 Main protease (Mpro) mediates the maturation cleavage of polyproteins during virus replication. Thus, inhibiting the role of spike RBD and Mpro of SARS-CoV-2 may affect the virus's viral entry and life cycle. Therefore, these proteins were chosen as potential targets for carrying out the in silico study. Though numerous drugs have been synthesized, most of their core structures or scaffolds originated from the natural products used in traditional medicines [6,7]. They have been a precious source of molecules with therapeutic potential. Among the diverse natural products, several phytochemicals were reported to treat infectious diseases caused by viruses, bacteria, and fungi [8-14]. Chromones are one such class of potent phytochemicals with widespread availability. Benzopyrone moiety in chromones has been recognized as a privileged structure owing to the variety of its pharmacological properties [15,16]. For instance, the chromones uncinoside A and uncinoside B derived from Selaginella uncinate were reported to exhibit potent antiviral activity against the respiratory syncytial virus with IC50 values of 13.8 and 20.8 μg mL-1, respectively [17]. Also, a recent in-silico study mentioned that among the various phytoconstituents in the genus aloe, chromones had the highest binding affinity towards the Mpro and spike RBD of SARS-Cov-2 [18]. Chromones were suggested for the early anti-inflammatory treatment of covid-19 [19]. An in silico study on the designed benzylidenechromanone, a chromone derivative, revealed that it has the potential to block SARS-CoV-2 Mpro [20]. A synthesized chromone derivative was docked against SARS-CoV-2 Mpro, and its binding efficiency was evaluated [21]. Also, the basic structure of chromone was studied against the wild-type spike protein and revealed that it could be a potential inhibitor [22]. To the best of our knowledge, there is “no extensive study” carried out on natural chromones from various plant sources against SARS-CoV-2 proteins, particularly Mpro and mutated spike RBDs.

Based on the remarkable potentials of chromones, a list of 173 natural chromones was identified from the literature [23] for screening against the SARS-CoV-2 Mpro and RBD of the wild type (which has no mutations) and its variants, namely, alpha, beta, gamma, and delta. The docking results of the Mpro were compared with drug molecules such as Nirmatrelvir, Dipyridamole, and the inhibitor N3, and that of the RBDs were compared with ceftazidime and kobophenol A. The above drugs were chosen based on their high binding affinity toward the respective proteins [24-27]. MD simulations were carried out for the best-docked complexes

for 100 ns to assess their stability and investigate the interactions. The g_mmpbsa calculations were performed to evaluate the binding free energy of the protein-ligand complexes. In addition, the residue-wise decomposition analysis of binding free energies was performed to identify the stabilizing and destabilizing residues of the protein. The pharmacokinetic properties and drug-likeness of the selected chromones were also analyzed.

2. Materials and Methods

2.1. Procuring of protein structures.

The 3D structure of the SARS-CoV-2 M^{pro} (PDB id: 6LU7), full spike protein or the RBD domains for different SARS-CoV-2 variants such as Wild type (PDB id: 6M0J); Alpha/N501Y (PDB id: 7MJN); Beta/K417N, E484K, N501Y (PDB id: 7NXA), Delta/T478K (PDB id: 7ORA), Delta/L452R (PDB id: 7ORB) and Gamma/K417T, E484K, N501Y (PDB id: 7NXB)) were obtained from the RCSB Protein Data Bank [28]. These structures were further processed by removing all other domains, antibodies, receptors (if complex), and other small molecules to get only the RBD domain from the full protein structures using Chimera [29].

2.2. Protein preparation.

The M^{pro} and spike RBD of each variant were prepared using the WHAT IF server [30]. The preparation includes performing missing side-chain modeling, regularization, and hydrogen additions when required. To get the native conformation, the prepared proteins were simulated for 20ns using the OPLS force field in GROMACS software (version 2019) [31]. The stable structure of each protein was extracted from the simulation trajectory and used for the docking program.

2.3. Ligand preparation.

The 3D structure of all the chromones was optimized using the GAUSSIAN09 software package [32] using the density functional theory-based method B3LYP and basis set 6-31G*. The keyword # opt freq b3lyp/6-31g* geom=connectivity was given in the route section for structural optimization. All the optimized structures were saved in pdb format and utilized for docking studies.

2.4. Molecular Docking.

The ligands were docked against each protein using PyRx, an open-source virtual screening software [33]. It uses the AutoDock Vina algorithm to execute molecular docking and calculate the binding affinities. The active site of each protein was obtained from the literature [5,34-37]. In some cases (7NXB), the active binding sites were obtained from the PDBsum web server [38] since the interacting residues were not mentioned directly in the literature. The interactions between the protein and ligand were visualized using the Protein-Ligand Interaction Profiler (PLIP) server [39].

2.5. Docking validation.

The PyMOL software was used to extract the inhibitor N3 and remove all the water molecules from the M^{pro} and save them separately in PDB file format [40]. The N3 inhibitor was re-docked with M^{pro} to validate the docking protocol used in this study.

2.6. MD simulations.

Docked complexes were simulated using GROMOS 96 54a7 force field in GROMACS software [41]. Ligand force field parameters were generated using an automated server PRODRG2 [42]. The complex was kept in the center of a cubic unit cell with a 1.0 nm distance from the edges of the box. The solvated system was prepared by filling the water SPC model. The solvated system was neutralized by replacing solvent molecules with Cl^- or Na^+ ions. In order to remove steric clashes that can lead to inappropriate geometry, the electro-neutral system was passed through an energy minimization step. The steepest descent method with a maximum of 50000 steps and force of <1000 kJ mol-1 nm -1 achieved the local minima. After energy minimization, the system had negative potential energy, which shows that the system was stable. Before equilibration, the ligand's heavy atoms were restrained, and the ligand was grouped with protein for temperature coupling. Canonical (NVT) equilibration stabilized the desired temperature (300K) of the system at 100ps. To stabilize the system for the desired pressure (1 bar), "isothermal-isobaric" (NPT) equilibration was used for the same time frame. To check the stability of well equilibrated system, restraints were released, and MD simulation was performed for 100ns. The PCA-based FEL plots for the topology files were produced by the MATLAB software (student version). RMSD, RMSF calculations were executed to check the stability of each complex during MD simulation. The radius of gyration was computed to observe the compactness of each docked complex. The H-bond calculation was carried out to check the number of interactions maintained during the simulation.

2.7. Binding Energy calculation.

Molecular mechanics Poisson-Boltzmann surface area (MM-PBSA) based method was used in g_mmpbsa to measure the binding energy between the protein and ligand [43]. The residue-wise decomposition analysis of binding free energies was performed to identify the stabilizing and destabilizing residues of the protein.

2.8. Analysis of pharmacokinetic properties.

The pharmacokinetic properties of the selected ligands were assessed using the SwissADME webserver [44]. The toxicity profile prediction was performed using the ProTox-II webserver [45]. The drug-likeness of the selected ligands was assessed using the webserver Molsoft [46].

3. Results and Discussion

3.1. Molecular docking.

The binding of a ligand to the protein of interest is the first and foremost step in drug discovery, and the molecular docking approach has been widely used to predict and investigate the binding nature of the ligand into the protein's binding pocket [47].

Therefore, in the present study, 173 natural chromones were docked against the active site of SARS-CoV-2 M^{pro} and spike RBD of wild type and its four variants of concern alpha, beta, gamma, and delta. For comparison, drugs like nirmatrelvir, dipyridamole, and the inhibitor N3 were docked against M^{pro}, and ceftazidime, kobophenol A were docked against each spike RBDs. Table 1 reveals the binding energy of the top hit chromones for the corresponding targets.

Table 1. The binding energy of chromones against SARS-CoV-2 M^{pro} and spike RBD of wild type and its variants.

Protein	PDB ID	Chromone	Binding energy (kcal/mol)
Main Protease	6LU7	Chromone-142	-9.1
Wild type	6M0J	Chromone-129	-7.8
Alpha	7MJN	Chromone -131	-8.1
Beta	7NXA	Chromone -131	-7.3
Gamma	7NXB	Chromone-132	-7.4
Delta-1/T478K	7ORA	Chromone-124	-7.8
Delta-2/L452R	7ORB	Chromone-132	-7.1

3.1.1. Main Protease.

The SARS-CoV-2 M^{pro} consists of three domains. Domain I (residues 8 to 101) and domain II (residues 102-184) had an antiparallel β-barrel structure, while domain III (residues 201-306) comprised five α-helices arranged into a largely antiparallel globular cluster. Domains II and III were connected by a long loop region (residues 185 to 200), and the substrate-binding site of SARS-CoV-2 M^{pro} was located between domains I and II. Inhibitors targeting the substrate-binding site were expected to have wide-spectrum activity against SARS-CoV-2 [34]. Therefore, the crystal structure of SARS-CoV-2 M^{pro} (PDB ID: 6LU7) inhibited by N3 in its substrate-binding pocket was utilized to analyze the binding ability of chromones in the same pocket.

After protein preparation, docking was performed between the chromones and M^{pro} by targeting its substrate-binding pocket. For comparison, the inhibitor N3 and potential SARS-CoV-2 therapeutic agents like Nirmatrelvir, Dipyridamole were also docked in the same region. Post-docking analysis revealed that Chromone-142 (7-O-(6'-Galloyl)-beta-D-glucopyranosyl-5-hydroxychromone) topped all the ligands with a binding energy of -9.1 kcal/mol. The details of all the interactions are given in Table S1 (in Supplementary Information). It interacts with the residues of domain I (THR25, THR26), domain II (GLY143, SER144, CYS145, MET165, GLU166), and loop region (GLN189, THR190, GLN192) through hydrophobic and hydrogen bonding interactions as shown in Figure 1. Interestingly, its binding energy was less than that of the reported drug molecules and native ligand N3, as seen in Table 2. Nirmatrelvir, an orally bioavailable SARS-CoV-2 M^{pro} inhibitor [24], had a binding energy of -8.4 kcal/mol. Dipyridamole, identified as a potent inhibitor of M^{pro} [21], had a binding energy of -7.9 kcal/mol. This signifies the remarkable binding potential of Chromone-142 against the M^{pro}.

Table 2. The binding energy of chromone-142 and reference molecules against the SARS-CoV-2 M^{pro}.

Ligands against M^{pro}	Binding energy (kcal/mol)
Chromone-142	-9.1
Nirmatrelvir	-8.4
N3 inhibitor	-8.0
Dipyridamole	-7.9

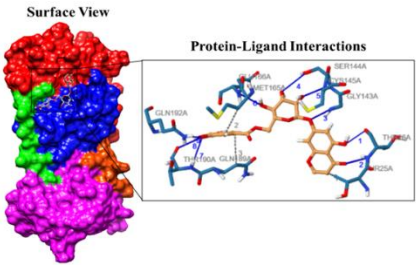

Figure 1. Interaction of Chromone-142 with M^{pro}. Colour indication: Red - Domain-I, Blue - Domain-II, Magenta - Domain-III, Orange - N-Terminal, Green - Loop region.

3.1.2. RBD of the spike protein.

The receptor-binding domain of the SARS-CoV-2 spike protein recognizes the cell surface of ACE2 receptor and paves the way for viral entry. It contains a twisted five-stranded antiparallel β sheet (β1, β2, β3, β4, and β7), which has short connecting helices and loops that constitute the core structure. Between the strands β4 and β7, there is an extended insertion comprising the short strands β5 and β6, α4 and α5 helices and loops. This extended insertion is called the Receptor Binding Motif (RBM). It holds most of the contacting residues of the viral spike that bind to ACE2 [5]. Therefore, inhibiting the spike RBD would be a rationale and vital approach for the entry inhibition of SARS-CoV-2. The spike RBD of wild type, alpha (N501Y), beta (K417N, E484K, N501Y), gamma (K417T, E484K, N501Y), delta (L452R), and delta (T478K) were docked with chromones by targeting their active site that involved in ACE2 binding. In addition, two drug molecules, Ceftazidime and Kobophenol A, were also docked against the RBDs for a comparative outlook.

The results of the docking study are presented in Table 1. Chromone-129 (5-Hydroxy-chromone-7-rutinoside) had bound to the wild-type spike RBD with the least binding energy of -7.8 kcal/mol. Chromone-131 (Sessilifoside) is bound to the spike RBD of alpha and beta variants with -8.1 and -7.3 kcal/mol, respectively. Chromone-132 (7"-O-beta-D-glucopyranosylsessilifoside) could interact with the spike RBD of both gamma and delta variant (L452R) with -7.4 and -7.1 kcal/mol, respectively. Chromone-124 (Corymbosins K4) exhibited -7.8 kcal/mol against the spike RBD of the delta variant (T478K).

From the interacting residues listed in Table S2, it was clear that chromones are bound to the active site of the wild type and its variant RBDs by establishing several interactions like hydrogen bonding, π-Cation, π- stacking, salt bridges, and hydrophobic interactions. The 2-D images of docking interactions between chromones and spike RBDs are depicted in Figure 2. Also, several residues were found common in all the complexes with their respective RBD-ACE2 interacting residues. This is an important factor in preventing viral entry since the key residues essential for binding with ACE2 would be already blocked by the chromones. So, they would no longer be available to recognize the cell surface of ACE2 receptors. Pharmacologically, if a ligand blocks a receptor's active site, its functional activity can be terminated [48]. Besides, the binding energy of all the top hit chromones was better than their corresponding drug-RBD interaction, as evident from Table 3. Ceftazidime was reported to be a potential drug to block spike protein-ACE2 interaction in vitro [26], and a combined computational and experimental report suggested that Kobophenol A could disrupt the interaction between ACE2 and the spike RBD [27]. From these results, it can be inferred that the potential of the selected chromones to block the active site of the spike RBDs is more promising.

Table 3. Binding energy (kcal/mol) of chromones and drug molecules against the SARS-CoV-2 spike RBDs.

RBD	Top Chromone	Ceftazidime	Kobophenol A
Wild type	-7.8	-5.6	-5.5
Alpha	-8.1	-6.3	-7.6
Beta	-7.3	-6.5	-6.1
Gamma	-7.4	-5.8	-6.1
Delta (T478K)	-7.8	-6.5	-5.8
Delta (L452R)	-7.1	-6.3	-6.0

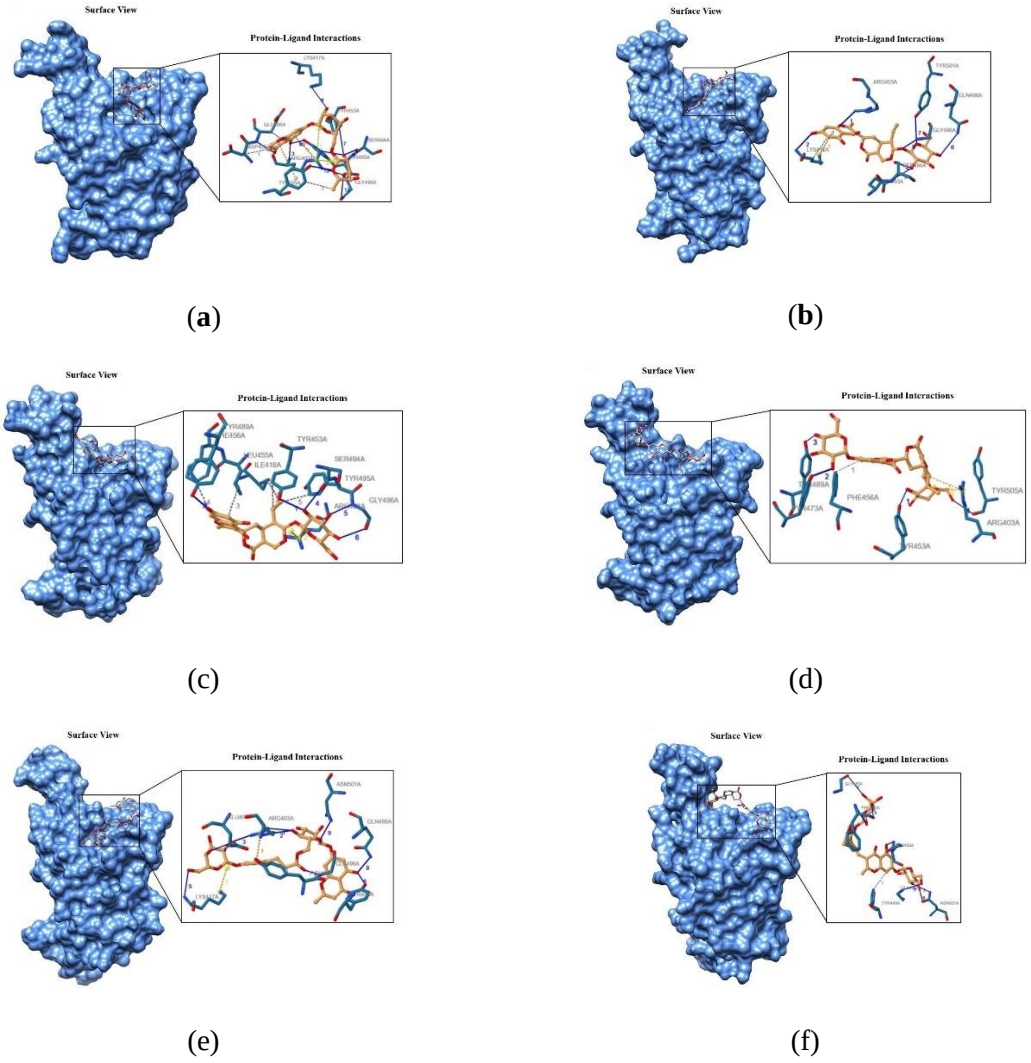

Figure 2. Interactions in the docked complexes **(a)** 6M0J-Chromone-129, **(b)** 7MJN-Chromone-131, **(c)** 7NXA-Chromone-131, **(d)** 7NXB-Chromone-132, **(e)** 7ORA-Chromone-124, **(f)** 7ORB-Chromone-132

3.1.3. Docking validation.

The validation of docking protocol is essential to examine their efficiency. For this, Mpro was selected since it is co-crystallized with a peptide inhibitor N3. The N3 from Mpro was extracted and re-docked into the active site of the protein using AutoDock Vina in PyRx user interface. It was performed manually by opening the co-crystallized complex in PyMOL, selecting the inhibitor N3 from Mpro, and saved in PDB file format. All the water molecules from Mpro were deleted and saved in PDB file format. Then, the inhibitor N3 was docked at the active site of Mpro to ensure that the inhibitor binds precisely to the active site cleft and shows less deviation compared to the actual co-crystallized complex. The peptide inhibitor bound precisely to the active site of Mpro with a binding energy of -8.0 kcal/mol. Then, the root mean square deviation (RMSD) was calculated by superimposing the re-docked complex

onto the reference co-crystallized complex using PyMOL. A low RMSD of 0.283 Å was observed, and the superimposition is represented in Figure 3. Shivanika *et al*. executed a similar re-docking of peptide inhibitor N3 against SARS-CoV-2 Mpro via AutoDock 4.2.6 and observed binding energy of -8.12 kcal/mol and superimposed the re-docked complex against reference co-crystallized N3-Mpro with an RMSD of 0.615 Å [49]. The interacted amino acid residues ASN 142, CYS 145, GLN189, HIS 41, LEU 141, MET 49 were found common with the present work.

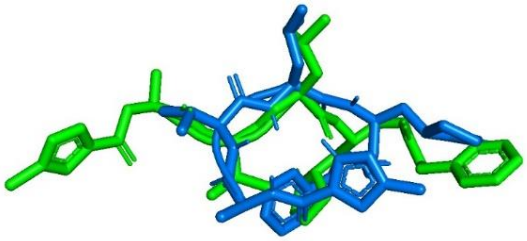

Figure 3. Superimposition of re-docked N3-M^{pro} (blue) against reference co-crystallized complex (green) in the active site using PyMOL.

The re-docked complex was superimposed against the reference co-crystallized N3-M^{pro} complex using LigPlot v.2.2 software. It is observed that it was superimposed completely onto the native co-crystallized complex with no adjustments. All the atoms of amino acids of both complexes were superimposed without any constraints. Overall, 13 amino acid residues are superimposed and encircled in red, as depicted in Figure 4. This proves the efficiency and validity of the docking protocol.

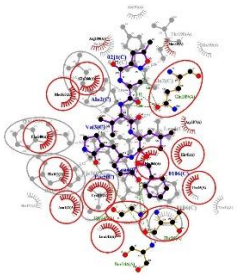

Figure 4. Superimposition of re-docked N3-M^{pro} onto reference co-crystallized complex using LigPlot v.2.2. Superimposed amino acids are encircled in red.

3.2. Structure-activity relationships.

From the structures of the selected chromones depicted in Figure 5, it was noted that all the ligands contained a minimum of one alpha-D-glucopyranose in their structures. This moiety involved hydrogen bonding with the targets to a significant extent, as evident from Figure 1 and Figure 2, and contributed significantly to the overall binding energy of the ligand. It's notable binding towards the targets could be due to the presence of multiple hydroxyl groups. Since proteins were composed of numerous -NH and -OH groups, the affinity of hydroxyl groups present in alpha-D-glucopyranose could facilitate the development of different interactions between the protein and ligand, including hydrogen bonding. Besides, the chromone ring present in all the top hit ligands interacted with the proteins through hydrogen bonds (using the carbonyl oxygen or hydroxyl group), and π-cation interaction (using the electron-rich benzene ring) contributed to the overall binding energy. In addition, the number of functionalities in the molecule played a crucial role in receptor binding. Multiple hydroxyl

groups are present in all the top-hit chromones, forming several hydrogen bonds with the respective protein.

On the other hand, molecules with fewer functionalities, like chromones 2, 25, 26, 37, 51, 118, and 139 (refer to Table S6 for the structures), had high binding energy against the targets ranging from -4.1 to -5.6 kcal/mol. This indicates the necessity for more potential functional groups in the ligand system. In a nutshell, it could be suggested that, while designing a ligand against SARS-CoV-2 Mpro and/or the spike RBDs, the alpha-D-glucopyranose and chromone ring may be introduced to get more and better interactions.

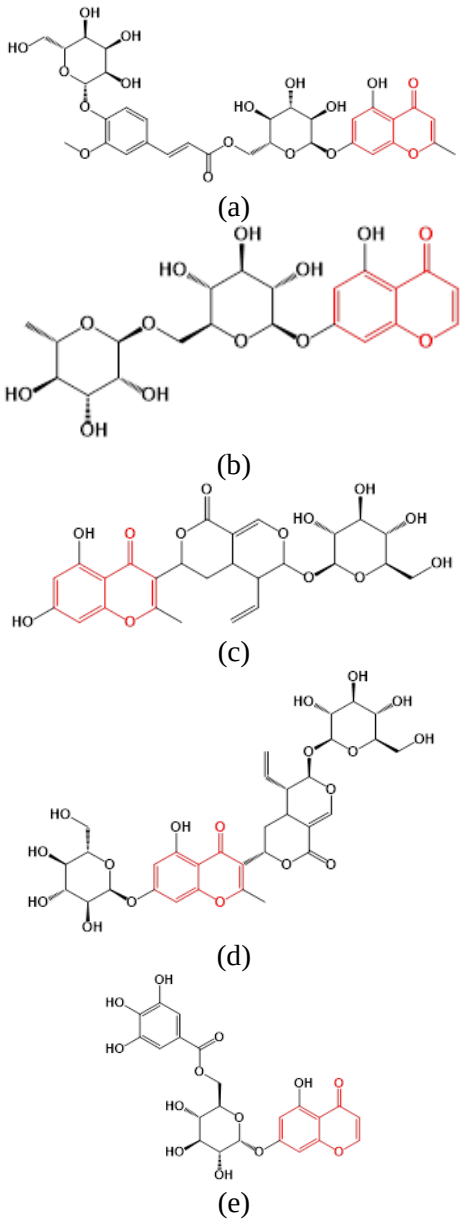

Figure 5. Structures of natural chromones that have the least binding energy against the SARS-CoV-2 M^{pro} and spike RBD of the wild type and its variants. The red color indicates the fundamental skeleton of chromones. **(a)** Corymbosins K4 (Chromone-124), **(b)** 5-Hydroxy-chromone-7-rutinoside (Chromone-129), **(c)** Sessilifoside (Chromone-131), **(d)** 7''-O-beta-D-glucopyranosylsessilifoside (Chromone-132), **(e)** 7-O-(6'-Galloyl)-beta-D-glucopyranosyl-5-hydroxychromone (Chromone-142)

3.3. MD Simulation.

In docking, the ligands and proteins were considered rigid and not flexible. But in a biological system, the molecules are flexible. Thus, their mode of binding and conformations

keep varying in response to the change in energy in the complex, molecules in its vicinity, and physiological conditions as a function of time. Therefore, it is essential to validate the docked complexes' stability [50]. In this study, the docked complexes were simulated for 100 ns, and their stability during the simulation was investigated. Also, the results of MD simulations and MM-PBSA of the complexes 6LU7-Chromone-142, 6M0J-Chromone-129, and 7ORB-Chromone-132 were replicated, as a representation to verify the consistency of the results and are presented in Figures S1, S2, S3, S4, and Table S5. The results were found to be consistent.

3.3.1. Free energy landscape analysis.

The function of a protein is regulated by its numerous conformational changes, which play a vital role in biological signal transmission. Also, the rigidity and flexibility of a protein, mainly that of the residues involved in binding, accredit a protein to be functional. So, to measure the overall movement and stability of the protein-ligand complex, the essential dynamics were utilized. PC1 and PC2 were computed by diagonalizing the covariance matrix of the eigenvector to indicate the critical subspaces where the most important protein dynamics would happen. The PCA-based FEL plots for the topology files were produced by the MATLAB software (student version). The plots in Figure 6 represent the minimal and maximum energy points for each complex. The deep blue color shows the lowest energy conformation, whereas the red color represents the highest energy conformation. The most stable structure for each complex (deep blue color) was extracted using MD trajectories and is presented in Figure 6. It is noted from the figure that all the ligands sustained their strength with the target by means of several hydrogen bonding and hydrophobic interactions with the key residues of the protein at the end of 100 ns in the PRODRG-derived topology file. The list of all the interactions is presented in Table S3. It shows that the interactions are thermodynamically favorable and assure the stability of the docked complexes.

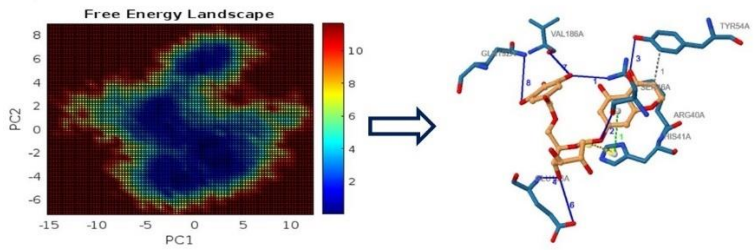

(**a**)

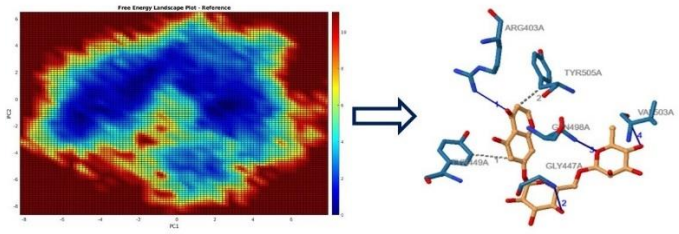

(**b**)

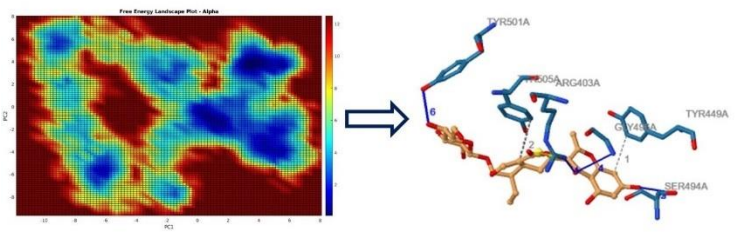

(**c**)

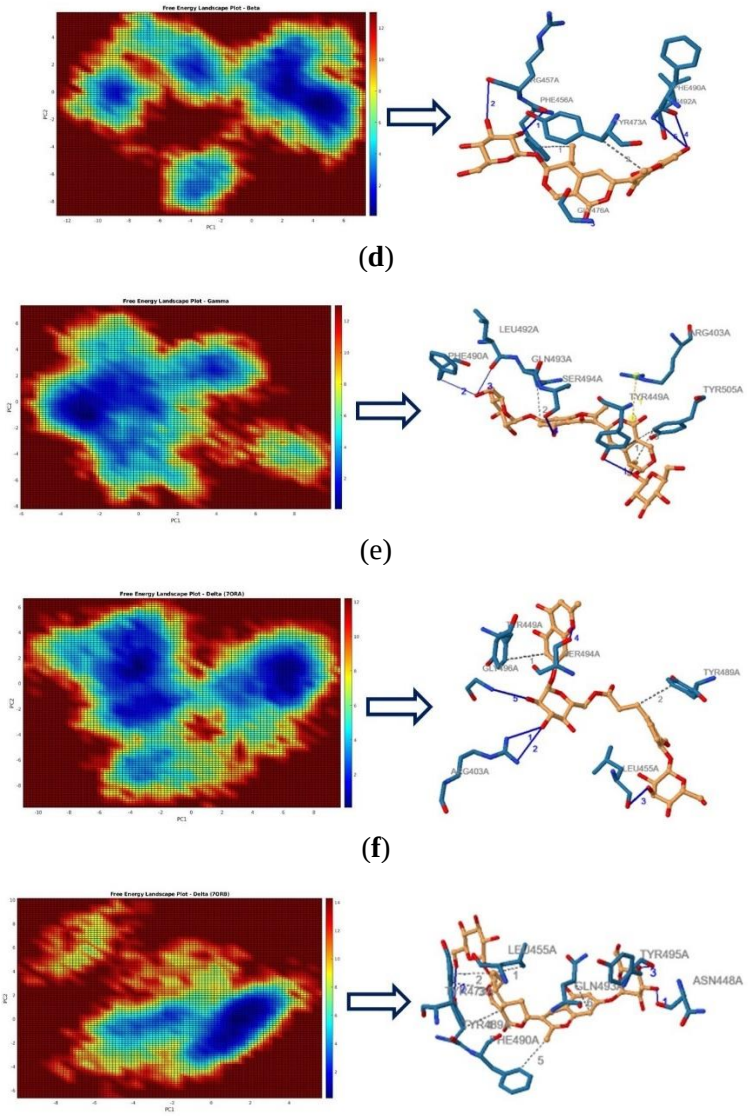

(**d**)

(e)

(**f**)

(**g**)

Figure 6. FEL plots and the corresponding minimum energy structures of the complexes **(a)** 6LU7-Chromone-142, **(b)** 6M0J-Chromone-129, **(c)** 7MJN-Chromone-131, **(d)** 7NXA-Chromone-131, **(e)** 7NXB-Chromone-132, **(f)** 7ORA-Chromone-124, **(g)** 7ORB-Chromone-132.

3.3.2. Stability analysis.

For a protein-ligand complex, the Root Mean Square Deviation (RMSD) of the protein backbone is a typical parameter. It illustrates their conformational stability in dynamic states by describing the system's equilibration. During simulation, the lower range of RMSD with consistent variation indicates the stability of a protein backbone [51]. Figure 7 shows the graphical representation of the RMSD of each docked complex. The duration of the simulation (0-100 ns) is given on the X-axis, and the RMSD (nm) is given on the Y-axis. The consistent RMSD plot of the complex 6LU7-Chromone-142 shows its stability throughout the simulation. The complex 6M0J-Chromone-129 showed a steady increase in RMSD value for the first 20 ns, then the RMSD trajectories equilibrated and maintained stable trajectories throughout the simulation. The complex 7MJN-Chromone-131 showed a steady increase in RMSD for the first ~40 ns, then it attained conformational stability, which was maintained till the end of the simulation.

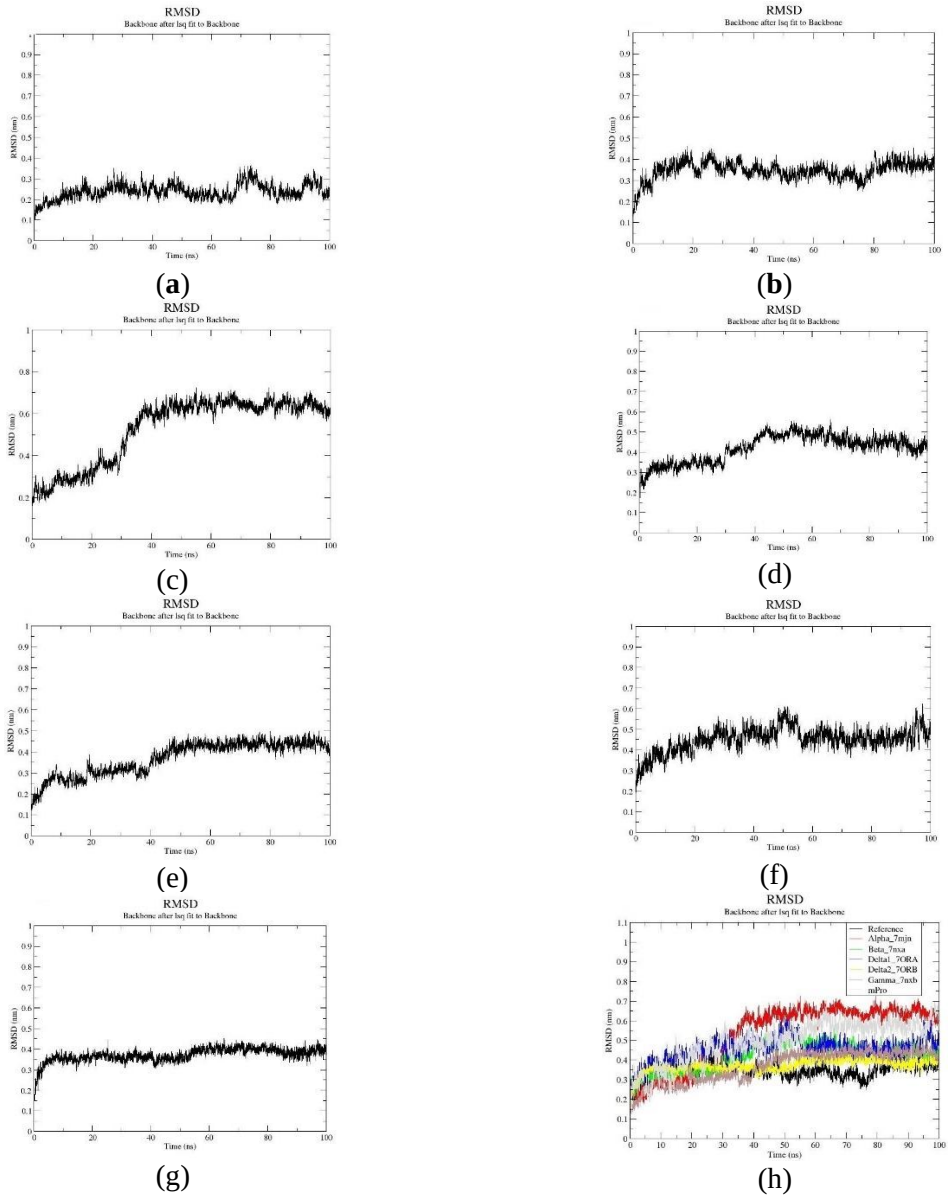

Figure 7. RMSD graph of the complexes **(a)** 6LU7-Chromone-142, **(b)** 6M0J-Chromone-129, **(c)** 7MJN-Chromone-131, **(d)** 7NXA-Chromone-131, **(e)** 7NXB-Chromone-132, **(f)** 7ORA-Chromone-124, **(g)** 7ORB-Chromone-132, **(h)** All protein-ligand complexes

Similarly, the complex 7NXA-Chromone-131 had a gradual increase in RMSD till ~40 ns and, reached conformational stability, and followed stable trajectories throughout the simulation. In the case of the complex of 7NXB-Chromone-132, it had a slow growth in RMSD till ~45 ns, and then it achieved conformational stability and maintained the same till the end of the simulation. The RMSD of the complex 7ORA-Chromone-124 maintained stable trajectories from 20 ns till the end of the simulation. Finally, an outstanding result was observed from the complex 7ORB-Chromone-132. It was conformationally more stable than all the other complexes since it achieved stability within 10 ns and remained stable throughout the simulation.

Root mean square fluctuation (RMSF) describes the conformational stability of individual residues in a macromolecular system. When the fluctuation values are less, the system is considered to be conformationally more stable. However, variation in the value of fluctuation implies structural complexity within the system, and it can be utilized to investigate the ligand binding to the target.

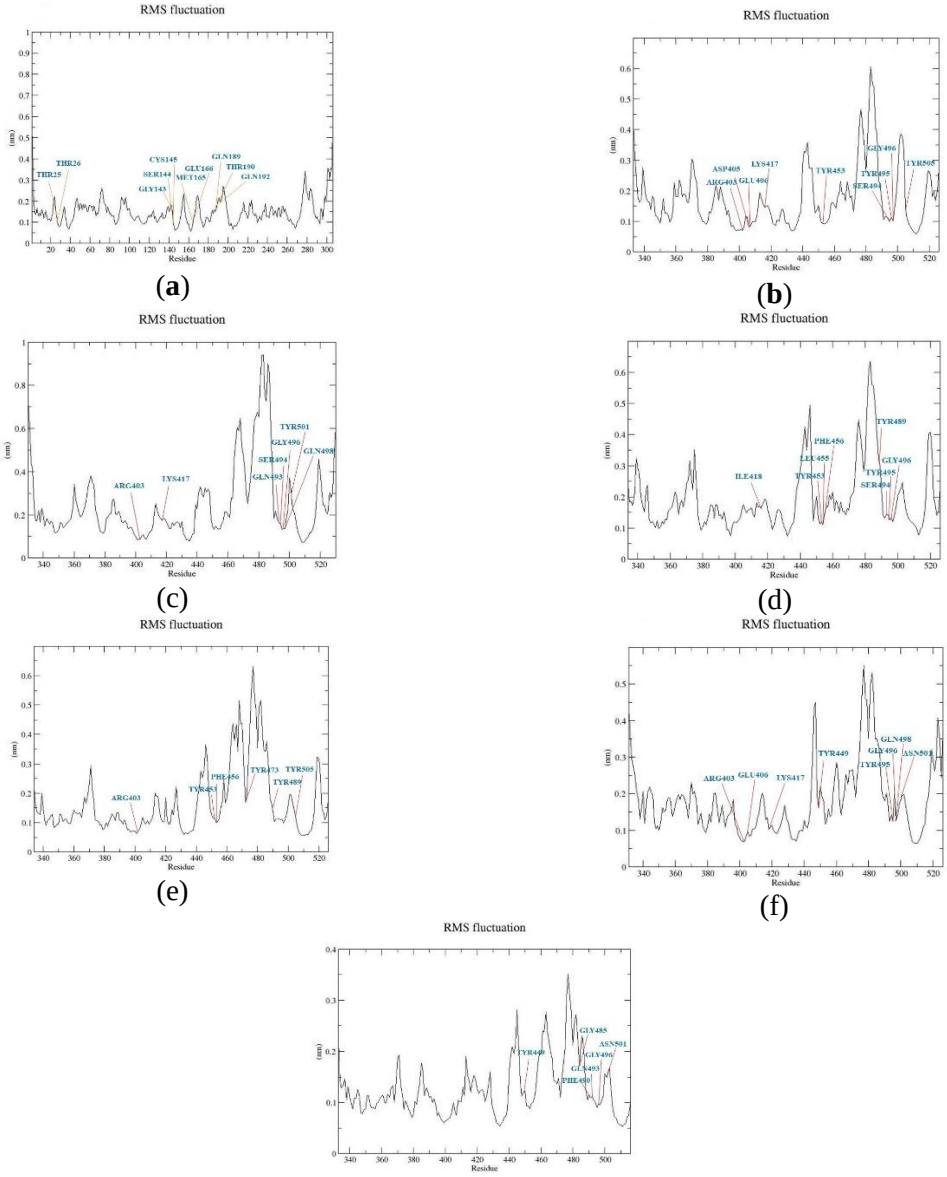

Figure 8. RMSF graph of the complexes **(a)** 6LU7-Chromone-142, **(b)** 6M0J-Chromone-129, **(c)** 7MJN-Chromone-131, **(d)** 7NXA-Chromone-131, **(e)** 7NXB-Chromone-132, **(f)** 7ORA-Chromone-124, **(g)** 7ORB-Chromone-132.

To examine the stability of the docked complexes, we observed their RMSF value at the interacting residues, as presented in Figure 8. It is clear from the figure that the interacting residues in all the docked complexes, except one, have an RMSF value of less than 0.2 nm. In the case of the complex 7NXA-Chromone-131, except TYR489, all the interacting residues have RMSF value of less than 0.2 nm. This indicates that the conformations have low flexibility, and protein-ligand interaction is adequately stable.

In brief, it is clear from the RMSD and RMSF plots of the docked complexes that the chromones did not diffuse away from the respective proteins during the simulation and showed a stable binding with them, indicating a good inhibition in the physiological environment. The time frames obtained after every 25 ns are depicted in Figure S5. It ensured that chromones were retained in the active site of the targets throughout the simulation and supported the stability of the docked complexes. The average RMSD of the SARS-CoV-2 M^{pro} and spike RBD of the wild type, alpha, beta, gamma, delta (7ORA), and delta (7ORB) complexes with corresponding ligands were 0.23, 0.34, 0.52, 0.41, 0.36, 0.45 and 0.37 nm respectively. These

values indicated that the studied docked complexes were stable, and the ligands had bound into the active pockets of the protein efficiently throughout the simulation.

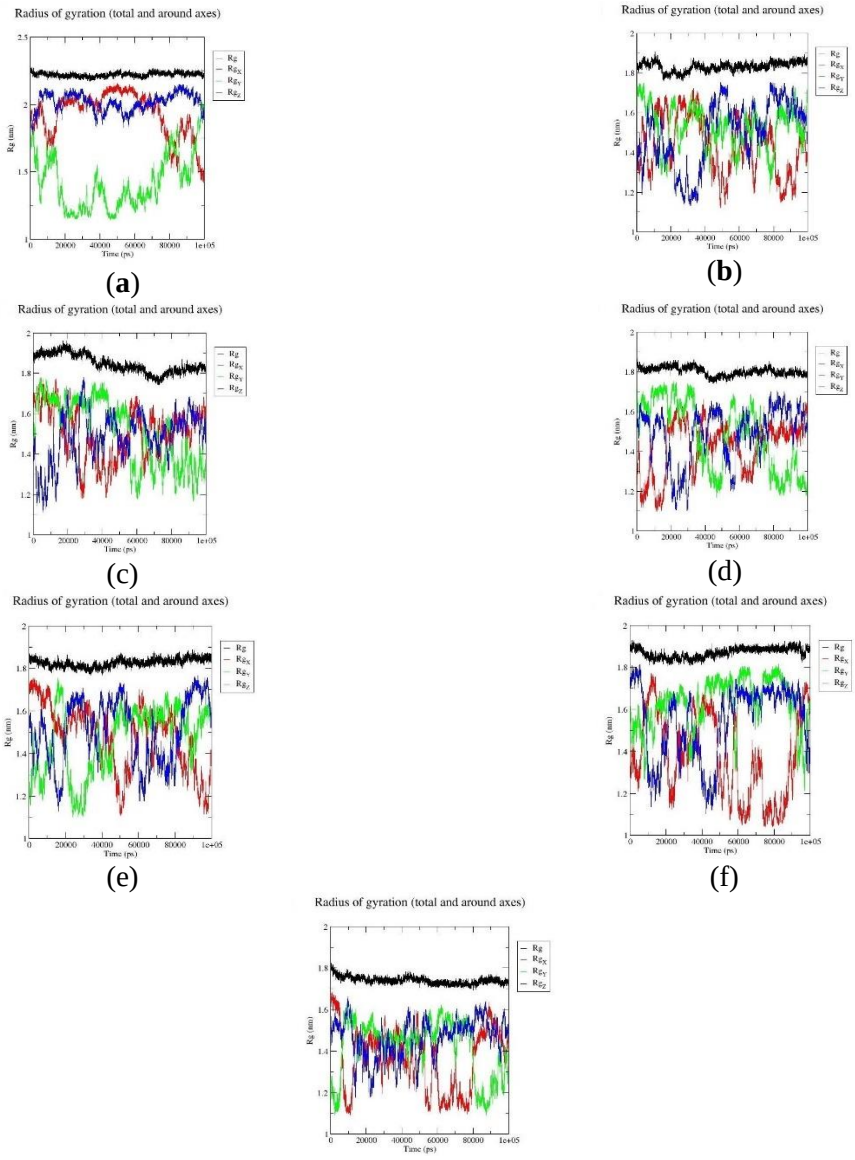

Figure 9. Radius of gyration plot of the complexes **(a)** 6LU7-Chromone-142, **(b)** 6M0J-Chromone-129, **(c)** 7MJN-Chromone-131, **(d)** 7NXA-Chromone-131, **(e)** 7NXB-Chromone-132, **(f)** 7ORA-Chromone-124, **(g)** 7ORB-Chromone-132

The radius of gyration (Rg) is the distance to express the strength of a system to bear the strain. It is quantified by measuring the distance between the center of mass and the rotational axis. It can be utilized to describe the conformational stability of a protein-ligand complex. A lesser Rg value and its fluctuation implies more conformational stability. It denotes that the center of mass of protein is closer to the axis of rotation. Also, the consistent value of Rg represents the stability throughout the simulation. Therefore, to examine the stability of protein-ligand complexes, we analyzed their radius of gyration (total and around axes), and the results are presented in Figure 9. It is clear from the plots that all the complexes have a steady Rg profile in the course of the simulation and did not deviate appreciably. Also, the Rg values of all the spike RBD complexes were found to be less than 2 nm, and that of M^{pro} complex is less than 2.5 nm. The lesser Rg values and lower degree of fluctuation indicate that the protein-ligand complexes are conformationally stable.

3.3.3. Hydrogen bonds.

In biological systems, hydrogen bonding is one of the key parameters for molecular interactions, binding stability, and backbone conformation. It provides the basis for molecular recognition by allowing explicitness and directionality to molecular interactions [52,53]. Therefore, we examined the formation of hydrogen bonds and their consistency at the active site of the proteins by capturing each frame generated during the MD simulation. These results are illustrated in Figure 10. It was observed that all the complexes contained an average of three hydrogen bonds during the entire run of the simulations. Particularly, the M^{pro} complex had maintained four hydrogen bonds with good consistency.

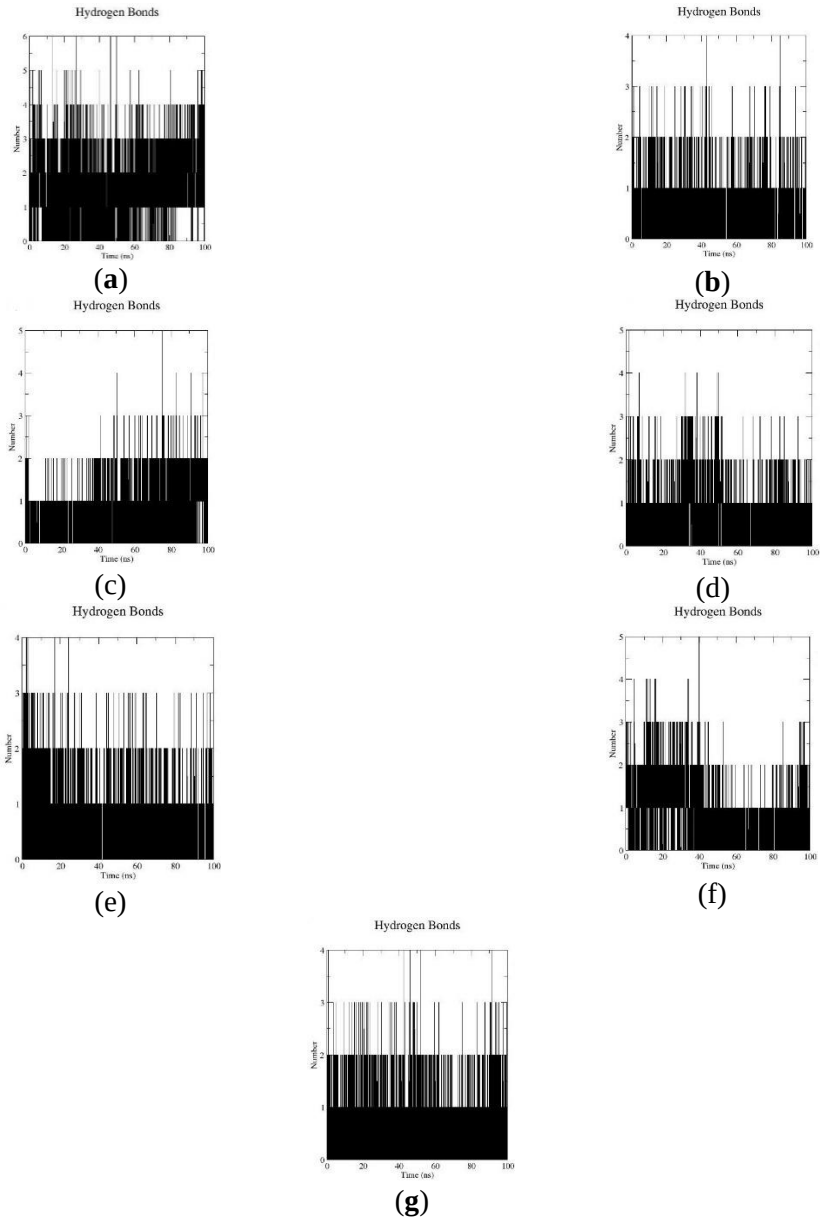

Figure 10. Hydrogen bond plot of the complexes **(a)** 6LU7-Chromone-142, **(b)** 6M0J-Chromone-129, **(c)** 7MJN-Chromone-131, **(d)** 7NXA-Chromone-131, **(e)** 7NXB-Chromone-132, **(f)** 7ORA-Chromone-124, **(g)** 7ORB-Chromone-132.

A fourth hydrogen bond has formed in all the RBD complexes, but they were short-lived in the whole process. The complexes of 6LU7-Chromone-142, 6M0J-Chromone-129, 7NXB-Chromone-132, and (g) 7ORB-Chromone-132 appear to have a relatively more intense hydrogen bond pattern than the rest. These results exhibited that the chromones formed a significant number of hydrogen bonds with the SARS-CoV-2 M^{pro} and spike RBDs, which

were maintained throughout the simulation. Also, it is well known that the intermolecular hydrogen bond interactions between the protein and ligand limit the binding site's internal movement and improve its stability [54]. Hence, the hydrogen bonds established by the chromones contributed significantly to the blockade of the protein's active site and the stability of the protein-ligand complexes throughout the simulation.

3.3.4. Binding free energy.

The binding ability of a ligand to the amino acid residues of a protein is crucial for the stability of the protein-ligand complex. It can be measured by performing binding free energy calculations.

$$\Delta G_{binding} = G_{complex} - (G_{protein} + G_{ligand}) \quad (1)$$

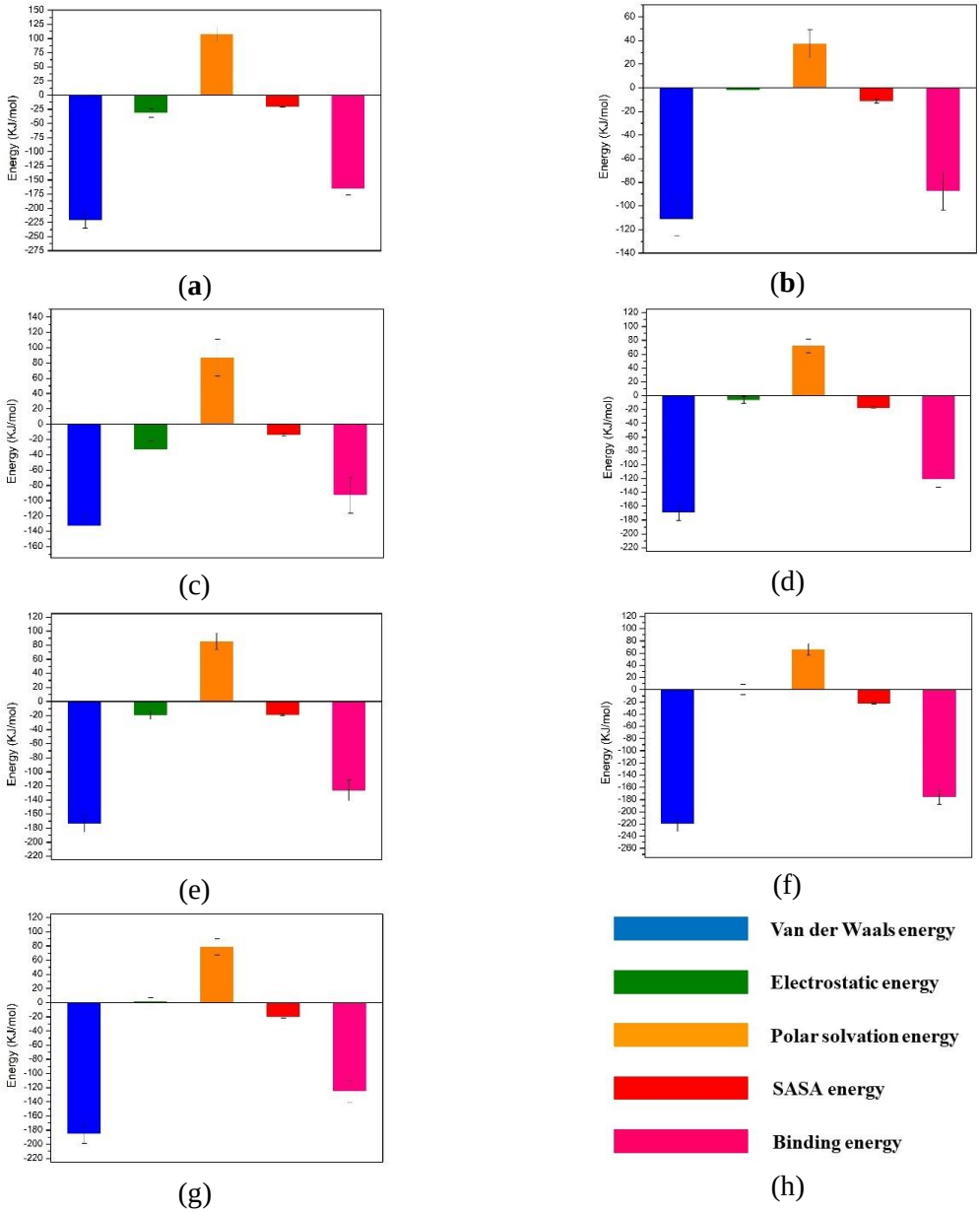

Figure 11. Depictions of Van der Waals energy, electrostatic energy, polar solvation energy, SASA energy, and binding energy, including their standard deviation values for the protein-ligand complex of **(a)** 6LU7-Chromone-142, **(b)** 6M0J-Chromone-129, **(c)** 7MJN-Chromone-131, **(d)** 7NXA-Chromone-131, **(e)** 7NXB-Chromone-132, **(f)** 7ORA-Chromone-124, **(g)** 7ORB-Chromone-132, **(h)** Colour code for different energies

Molecular Mechanics-Poisson Boltzmann Surface Area (MM-PBSA) calculation is a widely used method for calculating the binding free energy of protein-ligand complexes. The binding free energy of a protein-ligand complex is measured by the differences between the free energy of the complex and the unbound protein and ligand [55], as given in Equation (1). A high negative binding free energy implies the strong affinity of ligands towards the protein.

It is well-known that binding free energy is the sum of all nonbonded interactions. Here, we calculated the binding free energy of all the docked complexes using the MM-PBSA tool, which is illustrated with the standard deviation in Figure 11, and the values are presented in Table S2. The binding free energy of each complex is presented in Table 4. Among all the complexes, 6LU7-Chromone-142 and 7ORA-Chromone-124 were observed to exhibit the least binding free energy of -164.801 ± 11.619 kJ/mol and -175.418 ± 12.453 kJ/mol, respectively. The complexes 7NXA-Chromone-131, 7NXB-Chromone-132, and 7ORB-Chromone-132 have slight differences between their binding free energies with -120.960 ± 11.277 kJ/mol, -126.223 ± 14.693 kJ/mol, and -125.240 ± 15.246 kJ/mol, respectively. Among the complexes 6M0J-Chromone-129 and 7MJN-Chromone-131, the latter was found to be more stable with a value of -92.815 ± 23.718 kJ/mol, while the former has -87.232 ± 16.098 kJ/mol. The negative binding energies substantiated that all the docked complexes were stable during the simulation. The complexes' stability difference was accounted for through the residue-wise decomposition analysis, as presented in Fig. 12.

Table 4. The binding free energy of SARS-CoV-2 M^{pro} and spike RBD-Chromone complexes.

Complex	PDB ID	Simulation time (ns)	Binding Free Energy (kJ/mol)
6LU7-Chromone-142	6LU7	100	-164.801 ± 11.619
6M0J-Chromone-129	6M0J	100	-87.232 ± 16.098
7MJN-Chromone-131	7MJN	100	-92.815 ± 23.718
7NXA-Chromone-131	7NXA	100	-120.960 ± 11.277
7NXB-Chromone-132	7NXB	100	-126.223 ± 14.693
7ORA-Chromone-124	7ORA	100	-175.418 ± 12.453
7ORB-Chromone-132	7ORB	100	-125.240 ± 15.246

In the complex 6LU7-Chromone-142, stabilizing residues were more, while the destabilizing residues were relatively negligible. VAL42, MET49, GLY143, CYS145, and MET165 were the residues that contributed largely to the stability of the complex with binding energies -7.7264, -6.2145, -3.0944, -8.1559, -5.3701 kcal/mol, respectively. The interactions with these residues were responsible for the lesser binding free energy and better complex stability. Among the spike RBD complexes, the complex 7ORA-Chromone-124 has the least binding free energy since it has more stabilizing residues with high negative values. Notably, the residues TYR449, LEU455, PHE456, TYR473, TYR489, and PRO491 dominantly contributed to the stability of the complex with values -10.3889, -8.2176, -5.2916, -10.2737, -8.0408 and -6.6038 kcal/mol, respectively. Besides these stabilizing residues, ARG403 and GLU484 contribute unfavorably to the stability with values of +5.8866 and +3.0437 kcal/mol, respectively. This may be due to the repulsive forces between the ligand and the protein residues during the dynamics. On the other hand, in the 6M0J-Chromone-129 complex, where the binding free energy is relatively high, the number of stabilizing residues was lesser than that of the 7ORA-Chromone-124 complex. Some significantly stabilizing residues were GLY447, TYR449, PHE497, and TYR505, with values of -1.9165, -3.7536, -2.2192, and -8.6824 kcal/mol, respectively, while ARG403 predominantly destabilizes the complex with the value of +4.9859 kcal/mol. Similarly, in the complex 7MJN-Chromone-131, ARG403 contributes unfavorably to its stability with a +2.318 kcal/mol value. The complexes 7NXB-

Chromone-132, 7ORB-Chromone-132, and 7NXA-Chromone-131 have an almost similar number of significantly stabilizing residues ranging from 7 to 9 in each complex, while their highest magnitude goes around -7 kcal/mol. This explains the closeness in their binding energy values.

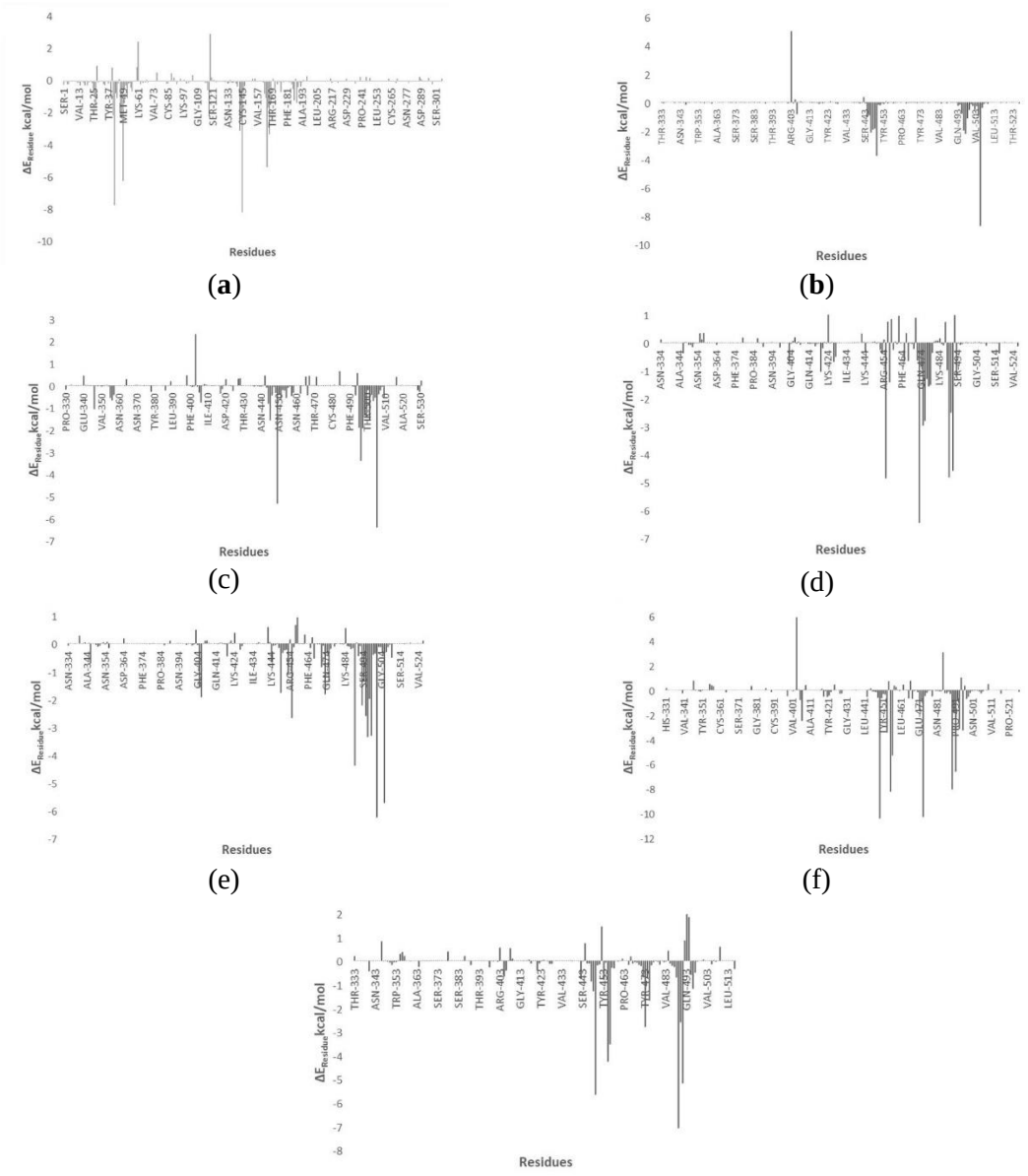

Figure 12. Residue-wise decomposition analysis of binding free energies for the complexes of **(a)** 6LU7-Chromone-142, **(b)** 6M0J-Chromone-129, **(c)** 7MJN-Chromone-131, **(d)** 7NXA-Chromone-131, **(e)** 7NXB-Chromone-132, **(f)** 7ORA-Chromone-124, **(g)** 7ORB-Chromone-132.

3.4. Pharmacokinetic properties.

3.4.1. ADME analysis.

Pharmacokinetics analyses and predicts the drug's movement into the human body once the medication is administered. It appraises the safety and efficacy of drug molecules to design suitable regimens. The pharmacokinetic properties of the selected chromones are presented in Table 5. All the molecules are predicted to be water-soluble. However, they may require intravenous administration due to their low gastrointestinal absorption, which may be due to their slightly increased molecular size. All the molecules are expected to have less CNS toxicity

and possible side effects since they are not BBB (blood-brain barrier) permeants. Inhibition of the isoenzymes (CYP1A2, CYP2C19, CYP2C9, CYP2D6, CYP3A4) is undoubtedly a major reason for pharmacokinetics-related drug-drug interactions leading to toxic or undesirable effects owing to the poor clearance and accumulation of the drug or its metabolite. None of the five chromones inhibit the cytochrome P450 (CYP) enzymes, ensuring their clearance from the human body.

Table 5. Pharmacokinetic properties of top hit chromones.

Parameters	Chromone-124	Chromone-129	Chromone-131	Chromone-132	Chromone-142
Water solubility	Soluble	Soluble	Soluble	Soluble	Soluble
GI absorption	Low	Low	Low	Low	Low
BBB permeant	No	No	No	No	No
P-gp substrate	Yes	No	Yes	Yes	Yes
CYP1A2 inhibitor	No	No	No	No	No
CYP2C19 inhibitor	No	No	No	No	No
CYP2C9 inhibitor	No	No	No	No	No
CYP2D6 inhibitor	No	No	No	No	No
CYP3A4 inhibitor	No	No	No	No	No

3.4.2. Toxicity profile and drug-likeness prediction.

Toxicity of different kinds, such as hepatotoxicity, carcinogenicity, immunotoxicity, mutagenicity, and cytotoxicity, were analyzed for the selected chromones. From the predicted toxicity profiles, as listed in Table 6, it is found that none of the compounds exhibit hepatotoxicity and carcinogenicity. Chromone-142 has no immunotoxicity, and the remaining compounds are predicted to be immunotoxic. Chromones-131, 132, and 142 are moderately safe concerning mutagenicity, and chromones-124 and 129 are expected to have only a moderate risk. Chromones-124, 129, 132, and 142 are moderately safe regarding cytotoxicity, and chromone-131 is predicted to have no cytotoxicity. From these results, chromones-124, 129, 131, 132, and 142 are classified with toxicity classes 5, 5, 4, 4, and 5, respectively. This indicates the less toxic nature of the top-hit chromones. Moreover, all the compounds have satisfactory LD50 values ranging from 1400-5000 mg/kg. Their drug-likeness model score is positive, and it is 0.36, 0.67, 1.19, 1.06, and 0.89 for chromones 124, 129, 131, 132, and 142, respectively. The graphical representation of the drug-likeness score of the top-hit ligands is depicted in Figure S6.

Table 6. Toxicity profile and drug-likeness prediction for the selected chromones.

Parameters	Chromone-124	Chromone-129	Chromone-131	Chromone-132	Chromone-142
Hepatotoxicity	HS	HS	HS	HS	HS
Carcinogenicity	HS	HS	HS	HS	HS
Immunotoxicity	HR	HR	HR	HR	HS
Mutagenicity	MR	MR	MS	MS	MS
Cytotoxicity	MS	MS	HS	MS	MS
Toxicity Class	V	V	IV	IV	V
LD_{50} (mg/kg)	5000	2500	1469	2000	2190
Drug-likeness model score	0.36	0.67	1.19	1.06	0.89

Note: HS- Highly Safe, MS- Moderately Safe, HR- High Risk, MR- Moderate Risk.
Lower toxicity class -V, moderate toxicity class – IV

4. Conclusions

A library of 173 natural chromones was screened in silico against the SARS-CoV-2 Mpro and spike RBD of the wild type and its variants. Docking studies unveiled that the selected chromones had substantial binding energy against the targets and performed better

than the drug molecules, such as nirmatrelvir, dipyridamole and the inhibitor N3 (for Mpro), ceftazidime and kobophenol A (for spike RBDs). The docking protocol is successfully validated by re-docking the inhibitor N3 with Mpro and superimposing the re-docked N3-Mpro onto the reference co-crystallized complex. Structure-activity relationships revealed that the alpha-D-glucopyranose and chromone ring moieties in the ligands contributed significantly to all complexes' binding energy. MD simulations validated the results achieved through molecular docking. The RMSD and RMSF graphs substantiated the stability of all the docked complexes. The Rg plots of the docked complexes ensured their compactness. Hydrogen bonds were well maintained between the chromones and their corresponding proteins. MM-PBSA calculations highlighted all the complexes' negative binding energy and emphasized the high stability of Mpro and delta variant (T478K) complexes with binding free energy -164.801 ± 11.619 and -175. 418 ± 12.453 kJ/mol, respectively. The pharmacokinetic profile and drug-likeness of the selected chromones were found satisfactory. Based on these results, we conclude that the selected chromones could be considered for in vitro studies to obtain promising leads for drug discovery against SARS-CoV-2.

Funding

This research was funded by the Science and Engineering Research Board, Government of India (File No. EEQ/2018/000428).

Acknowledgments

Premkumar G acknowledges Pondicherry University for providing University Research Fellowship.

Conflicts of Interest

The authors report that there are no competing interests to declare.

References

1. WHO Coronavirus (COVID-19) Dashboard. Available online: https://covid19.who.int/
2. Classification of Omicron (B.1.1.529): SARS-CoV-2 Variant of Concern. https://www.who.int/news/item/26-11-2021-classification-of-omicron-(b.1.1.529)-sars-cov-2-variant-of-concern
3. Chen, J.; Wang, R.; Wang, M.; Wei, G.W. Mutations Strengthened SARS-Cov-2 Infectivity. *J. Mol. Biol.* **2020,** *432*, 5212-26, https://pubmed.ncbi.nlm.nih.gov/32710986/.
4. Cui, W.; Yang, K.; Yang, H. Recent Progress In The Drug Development Targeting SARS-Cov-2 Main Protease As Treatment For COVID-19. *Front. Mol. Biosci.* **2020**, *7*, 1-10, https://doi.org/10.3389/fmolb.2020.616341.
5. Lan, J.; Ge, J.; Yu, J.; Shan, S.; Zhou, H.; Fan, S.; Zhang, Q.; Shi, X.; Wang, Q.; Zhang, L.; Wang, X. Structure Of The SARS-Cov-2 Spike Receptor-Binding Domain Bound To The ACE2 Receptor. *Nature*. **2020,** *7807*, 215-20. https://doi.org/10.1038/s41586-020-2180-5.
6. Newman, D.J.; Cragg, G.M. Natural Products as Sources of New Drugs Over the Last 25 Years. *J. Nat. Prod.* **2007,** *70*, 461-77. https://doi.org/10.1021/np068054v.
7. Newman, D.J.; Cragg, G.M. Natural Products as Sources of New Drugs From 1981 to 2014. *J. Nat. Prod.* **2016,** *79*, 629-61, https://doi.org/10.1021/acs.jnatprod.5b01055.
8. Ben-Shabat, S.; Yarmolinsky, L.; Porat, D.; Dahan, A. Antiviral Effect of Phytochemicals From Medicinal Plants: Applications and Drug Delivery Strategies. *Drug Deliv. Transl. Res.* **2020,** *10*, 354-67, https://doi.org/10.1007/s13346-019-00691-6.

9. Mahady, G.B. Medicinal Plants for the Prevention and Treatment of Bacterial Infections. *Curr. Pharm. Des.* **2005**, *19*, 2405-27. https://doi.org/10.2174/1381612054367481.
10. Kumar, A.; Choudhir, G.; Shukla, S. K.; Sharma, M.; Tyagi, P.; Bhushan, A.; Rathore, M. Identification of Phytochemical Inhibitors against Main Protease of COVID-19 Using Molecular Modeling Approaches. *J. Biomol. Struct. Dyn.* **2020**, *39*, 3760–3770. https://doi.org/10.1080/07391102.2020.1772112.
11. Jakhmola, S.; Hazarika, Z.; Jha, A.N.;, Jha, H.C. *In Silico* Analysis of Antiviral Phytochemicals Efficacy Against Epstein–Barr Virus Glycoprotein H. *J. Biomol. Struct. Dyn.* **2022**, *40*, 5372-85. https://doi.org/10.1080/07391102.2020.1871074.
12. Sultana, A.; Hossain, M.J.; Kuddus, M.R.; Rashid, M.A.; Zahan, M.S.; Mitra S.; Roy, A.; Alam, S.; Sarker, M.M.; Naina, M.I. Ethnobotanical Uses, Phytochemistry, Toxicology, And Pharmacological Properties of Euphorbia Neriifolia Linn. Against Infectious Diseases: A Comprehensive Review. *Molecules* **2022,** *27*, 4374. https://doi.org/10.3390/molecules27144374.
13. Yadav, H.; Mahalvar, A.; Pradhan, M.; Yadav, K.; Sahu, K.K.; Yadav, R. Exploring the Potential of Phytochemicals and Nanomaterial: A Boon to Antimicrobial Treatment. *Medicine in Drug Discovery* **2023**, *23*, 100151. https://doi.org/10.1016/j.medidd.2023.100151.
14. Li, Y.; Wu, Y.; Li, S.; Li, Y.; Zhang, X.; Shou, Z.; Gu, S.; Zhou, C.; Xu, D.; Zhao, K.; Tan, S. Identification of Phytochemicals in Qingfei Paidu Decoction for the Treatment of Coronavirus Disease 2019 by Targeting the Virus-Host Interactome. *Biomed. Pharmacother.* **2022**, *156*, 113946. https://doi.org/10.1016/j.biopha.2022.113946.
15. Pratap, R.; Ram, V. J. Natural and Synthetic Chromenes, Fused Chromenes, and Versatility of Dihydrobenzo[*h*]Chromenes in Organic Synthesis. *Chem. Rev.* **2014**, *114*, 10476–10526. https://doi.org/10.1021/cr500075s.
16. Keri, R. S.; Budagumpi, S.; Pai, R. K.; Balakrishna, R. G. Chromones as a Privileged Scaffold in Drug Discovery: A Review. *Eur. J. Med. Chem.* **2014**, *78*, 340–374. https://doi.org/10.1016/j.ejmech.2014.03.047.
17. Ma, L.-Y.; Ma, S.-C.; Wei, F.; Lin, R.-C.; But, P. P.-H.; Lee, S. H.-S.; Lee, S. F. Uncinoside A and B, Two New Antiviral Chromone Glycosides from *Selaginella Uncinata*. *Chem. Pharm. Bull.* **2003**, *51*, 1264–1267. https://doi.org/10.1248/cpb.51.1264.
18. Abouelela, M. E.; Assaf, H. K.; Abdelhamid, R. A.; Elkhyat, E. S.; Sayed, A. M.; Oszako, T.; Belbahri, L.; El Zowalaty, A. E.; Abdelkader, M. S. Identification of Potential SARS-COV-2 Main Protease and Spike Protein Inhibitors from the Genus Aloe: An *In-Silico* Study for Drug Development. *Molecules* **2021**, *26*, 1767. https://doi.org/10.3390/molecules26061767.
19. Sestili, P.; Stocchi, V. Repositioning Chromones for Early Anti-Inflammatory Treatment of Covid-19. *Front. Pharmacol.* **2020**, *11*, 1-5, https://doi.org/10.3389/fphar.2020.00854.
20. Sepay, N.; Sepay, N.; Al Hoque, A.; Mondal, R.; Halder, U. C.; Muddassir, M. In Silico Fight against Novel Coronavirus by Finding Chromone Derivatives as Inhibitor of Coronavirus Main Proteases Enzyme. *Struct. Chem.* **2020**, *31*, 1831–1840. https://doi.org/10.1007/s11224-020-01537-5.
21. Jenepha Mary, S. J.; Pradhan, S.; James, C. Molecular Structure, NBO Analysis of the Hydrogen-Bonded Interactions, Spectroscopic (FT–IR, Ft–Raman), Drug Likeness and Molecular Docking of the Novel Anti Covid-2 Molecule (2E)-N-Methyl-2-[(4-Oxo-4h-Chromen-3-Yl)Methylidene]-Hydrazinecarbothioamide (Dimer) - Quantum Chemical Approach. *Spectrochimica Acta Part A: Molecular Spectroscopy* **2021**, *251*, 119388. https://doi.org/10.1016/j.saa.2020.119388.
22. Sharma, V.; Panwar, A.; Sankhyan, A.; Ram, G.; Sharma, A. K. Exploring the Potential of Chromones as Inhibitors of Novel Coronavirus Infection Based on Molecular Docking and Molecular Dynamics Simulation Studies. *Biointerface Res. Appl. Chem.* **2022**, *13*, 104, https://biointerfaceresearch.com/wp-content/uploads/2022/03/BRIAC132.104.pdf.
23. Semwal, R. B.; Semwal, D. K.; Combrinck, S.; Viljoen, A. Health Benefits of Chromones: Common Ingredients of Our Daily Diet. *Phytochem Rev.* **2020**, *19*, 761–785. https://doi.org/10.1007/s11101-020-09681-w.
24. Owen, D. R.; Allerton, C. M.; Anderson, A. S.; Aschenbrenner, L.; Avery, M.; Berritt, S.; Boras, B.; Cardin, R. D.; Carlo, A.; Coffman, K. J.; Dantonio, A.; Di, L.; Eng, H.; Ferre, R. A.; Gajiwala, K. S.; Gibson, S. A.; Greasley, S. E.; Hurst, B. L.; Kadar, E. P.; Kalgutkar, A. S.; Lee, J. C.; Lee, J.; Liu, W.; Mason, S. W.; Noell, S.; Novak, J. J.; Obach, R. S.; Ogilvie, K.; Patel, N. C.; Pettersson, M.; Rai, D. K.; Reese, M. R.; Sammons, M. F.; Sathish, J. G.; Singh, R. S.; Steppan, C. M.; Stewart, A. E.; Tuttle, J. B.; Updyke, L.; Verhoest, P. R.; Wei, L.; Yang, Q.; Zhu, Y. An Oral SARS-COV-2 m pro Inhibitor Clinical Candidate for the Treatment of COVID-19. *Science* **2021**, *374*, 1586–1593. https://doi.org/10.1126/science.abl4784.

25. Li, Z.; Li, X.; Huang, Y.-Y.; Wu, Y.; Liu, R.; Zhou, L.; Lin, Y.; Wu, D.; Zhang, L.; Liu, H.; Xu, X.; Yu, K.; Zhang, Y.; Cui, J.; Zhan, C.-G.; Wang, X.; Luo, H.-B. Identify Potent SARS-COV-2 Main Protease Inhibitors via Accelerated Free Energy Perturbation-Based Virtual Screening of Existing Drugs. *Proc. Natl. Acad. Sci.* **2020**, *117*, 27381–27387. https://doi.org/10.1073/pnas.2010470117.
26. Lin, C. D.; Li, Y.; Zhang, Y. B.; Liu, Z. Y.; Mu, X.; Gu, C.; Liu, J.; Li, Y.; Li, G. H.; Chen, J. F. Ceftazidime Is a Potential Drug to Inhibit SARS-COV-2 Infection in Vitro by Blocking Spike Protein–ace2 Interaction. *Signal Transduct Target Ther.* **2021**, *6*. https://doi.org/10.1038/s41392-021-00619-y.
27. Gangadevi, S.; Badavath, V. N.; Thakur, A.; Yin, N.; De Jonghe, S.; Acevedo, O.; Jochmans, D.; Leyssen, P.; Wang, K.; Neyts, J.; Yujie, T.; Blum, G. Kobophenol a Inhibits Binding of Host Ace2 Receptor with Spike RBD Domain of SARS-COV-2, a Lead Compound for Blocking COVID-19. *J. Phys. Chem. Lett.* **2021**, *12*, 1793–1802. https://doi.org/10.1021/acs.jpclett.0c03119.
28. Berman, H. M. The Protein Data Bank. *Nucleic Acids Res.* **2000**, *28*, 235–242. https://www.rcsb.org/.
29. Pettersen, E. F.; Goddard, T. D.; Huang, C. C.; Couch, G. S.; Greenblatt, D. M.; Meng, E. C.; Ferrin, T. E. UCSF Chimera-a Visualization System for Exploratory Research and Analysis. *J. Comput. Chem.* **2004**, *25*, 1605–1612. https://doi.org/10.1002/jcc.20084.
30. Vriend, G. What If: A Molecular Modeling and Drug Design Program. *J. Mol. Graph.* **1990**, *8*, 52–56. https://doi.org/10.1016/0263-7855(90)80070-V.
31. Berendsen, H. J. C.; van der Spoel, D.; van Drunen, R. Gromacs: A Message-Passing Parallel Molecular Dynamics Implementation. *Comput. Phys. Commun.* **1995**, *91*, 43–56. https://doi.org/10.1016/0010-4655(95)00042-E.
32. Frisch, M. J.; Trucks, G. W.; Schlegel, H. B.; Scuseria, G. E.; Robb, M. A.; Cheeseman, J. R.; Scalmani, G.; Barone, V., Mennucci, B.; Petersson, G. A.; Nakatsuji, H.; Caricato, M.; Li, X.; Hratchian, H. P.; Izmaylov, A. F.; Bloino, J.; Zheng, G.; Sonnenberg, J. L.; Hada, M.; Ehara, M.; Toyota, K.; Fukuda, R.; Hasegawa, J.; Ishida, M.; Nakajima, T.; Honda, Y.; Kitao, O.; Nakai, H.; Vreven, T.; Montgomery, J. A.; Jr; Peralta, J. E.; Ogliaro, F.; Bearpark, M.; Heyd, J. J.; Brothers, E.; Kudin, K. N.; Staroverov, V. N.; Keith, T.; Kobayashi, R.; Normand, J.; Raghavachari, K.; Rendell, A.; Burant, J. C.; Iyengar, S. S.; Tomasi, J.; Cossi, M.; Rega, N.; Millam, J. M.; Klene, M.; Knox, J. E.; Cross, J. B.; Bakken, V.; Adamo, C.; Jaramillo, J.; Gomperts, R.; Stratmann, R. E.; Yazyev, O.; Austin, A.J.; Cammi, R.; Pomelli, C.; Ochterski, J.W.; Martin, R. L.; Morokuma, K.; Zakrzewski, V. G.; Voth, G. A.; Salvador, P.; Dannenberg, J. J.; Dapprich, S.; Daniels, A. D.; Farkas, O.; Foresman, J. B.; Ortiz, J. V.; Cioslowski, J.; D. J. Fox. **2010**, Gaussian, Inc., Wallingford CT, . https://www.scirp.org/(S(351jmbntvnsjt1aadkozje))/reference/referencespapers.aspx?referenceid=1989943.
33. Dallakyan, S.; Olson, A. J. Small-Molecule Library Screening by Docking with Pyrx. *Methods Mol. Biol.* **2014**, 243–250. https://doi.org/10.1007/978-1-4939-2269-7_19.
34. Jin, Z.; Du, X.; Xu, Y.; Deng, Y.; Liu, M.; Zhao, Y.; Zhang, B.; Li, X.; Zhang, L.; Peng, C.; Duan, Y.; Yu, J.; Wang, L.; Yang, K.; Liu, F.; Jiang, R.; Yang, X.; You, T.; Liu, X.; Yang, X.; Bai, F.; Liu, H.; Liu, X.; Guddat, L. W.; Xu, W.; Xiao, G.; Qin, C.; Shi, Z.; Jiang, H.; Rao, Z.; Yang, H. Structure of M^{pro} from SARS-COV-2 and Discovery of Its Inhibitors. *Nature* **2020**, *582*, 289–293. https://doi.org/10.1038/s41586-020-2223-y.
35. Zhu, X.; Mannar, D.; Srivastava, S. S.; Berezuk, A. M.; Demers, J.-P.; Saville, J. W.; Leopold, K.; Li, W.; Dimitrov, D. S.; Tuttle, K. S.; Zhou, S.; Chittori, S.; Subramaniam, S. Cryo-Electron Microscopy Structures of the N501Y SARS-COV-2 Spike Protein in Complex with ACE2 and 2 Potent Neutralizing Antibodies. *PLoS Biol.* **2021**, *19*. https://doi.org/10.1371/journal.pbio.3001237.
36. Khan, A.; Zia, T.; Suleman, M.; Khan, T.; Ali, S. S.; Abbasi, A. A.; Mohammad, A.; Wei, D. Q. Higher Infectivity of the Sars-Cov-2 New Variants Is Associated with K417N/t, E484K, and n501y Mutants: An Insight from Structural Data. *J. Cell. Physiol.* **2021**, *236*, 7045–7057. https://doi.org/10.1002/jcp.30367.
37. Khan., A.; Wei, D. Q.; Kousar, K.; Abubaker, J.; Ahmad, S.; Ali, J.; Al-Mulla, F.; Ali, S. S.; Nizam-Uddin, N.; Mohammad Sayaf, A.; Mohammad, A. Preliminary Structural Data Revealed That the Sars-Cov-2 B.1.617 Variant's RBD Binds to ACE2 Receptor Stronger than the Wild Type to Enhance the Infectivity. *ChemBioChem* **2021**, *22*, 2641–2649. https://doi.org/10.1002/cbic.202100191.
38. Laskowski, R. A.; Hutchinson, E. G.; Michie, A. D.; Wallace, A. C.; Jones, M. L.; Thornton, J. M. PDBsum: A Web-Based Database of Summaries and Analyses of All PDB Structures. *Trends Biochem. Sci.* **1997**, *22*, 488–490. https://doi.org/10.1016/S0968-0004(97)01140-7.
39. Salentin, S.; Schreiber, S.; Haupt, V. J.; Adasme, M. F.; Schroeder, M. PLIP: Fully Automated Protein–Ligand Interaction Profiler. *Nucleic Acids Res.* **2015**, *43*. https://doi.org/10.1093/nar/gkv315.

40. Schrodinger LL. The PyMOL molecular graphics system. Version. **2010** *5*. https://pymol.org/2/.
41. Schmid, N.; Eichenberger, A. P.; Choutko, A.; Riniker, S.; Winger, M.; Mark, A. E.; van Gunsteren, W. F. Definition and Testing of the Gromos Force-Field Versions 54A7 and 54B7. *Eur. Biophys. J.* **2011**, *40*, 843–856. https://doi.org/10.1007/s00249-011-0700-9.
42. Schüttelkopf, A. W.; van Aalten, D. M. *Prodrg*: A Tool for High-Throughput Crystallography of Protein–Ligand Complexes. *Acta Crystallogr. D Biol. Crystallogr.* **2004**, *60*, 1355–1363. https://doi.org/10.1107/S0907444904011679.
43. Kumari, R.; Kumar, R.; Lynn, A. *g_mmpbsa*—a Gromacs Tool for High-Throughput MM-PBSA Calculations. *J. Chem. Inf. Model.* **2014**, *54*, 1951–1962. https://doi.org/10.1021/ci500020m.
44. Daina, A.; Michielin, O.; Zoete, V. SwissADME: A Free Web Tool to Evaluate Pharmacokinetics, Drug-Likeness and Medicinal Chemistry Friendliness of Small Molecules. *Sci. Rep.* **2017**, *7*. https://www.nature.com/articles/srep42717.
45. Banerjee, P.; Eckert, A. O.; Schrey, A. K.; Preissner, R. Protox-II: A Webserver for the Prediction of Toxicity of Chemicals. *Nucleic Acids Res.* **2018**, *46*. https://academic.oup.com/nar/article/46/W1/W257/4990033.
46. Drug-Likeness and molecular property prediction. Available online: http://molsoft.com/mprop/
47. Jorgensen, W. L. The Many Roles of Computation in Drug Discovery. *Science* **2004**, *303*, 1813–1818. https://doi.org/10.1126/science.1096361.
48. Salman, S.; Shah, F. H.; Idrees, J.; Idrees, F.; Velagala, S.; Ali, J.; Khan, A. A. Virtual Screening of Immunomodulatory Medicinal Compounds as Promising Anti-SARS-Cov-2 Inhibitors. *Future Virol.* **2020**, *15*, 267–275. https://doi.org/10.2217/fvl-2020-0079.
49. Shivanika, C.; Kumar, D.; Ragunathan, V.; Tiwari, P.; A., S.; P, B. D. Molecular Docking, Validation, Dynamics Simulations, and Pharmacokinetic Prediction of Natural Compounds against the SARS-COV-2 Main-Protease. *J. Biomol. Struct. Dyn.* **2020**, *40*, 585–611. https://www.tandfonline.com/doi/full/10.1080/07391102.2020.1815584.
50. Mhatre, S.; Gurav, N.; Shah, M.; Patravale, V. Entry-Inhibitory Role of Catechins against SARS-COV-2 and Its UK Variant. *Comput. Biol. Med.* **2021**, *135*, 104560. https://doi.org/10.1016/j.compbiomed.2021.104560.
51. Sinha, S. K.; Prasad, S. K.; Islam, M. A.; Gurav, S. S.; Patil, R. B.; AlFaris, N. A.; Aldayel, T. S.; AlKehayez, N. M.; Wabaidur, S. M.; Shakya, A. Identification of Bioactive Compounds from *Glycyrrhiza Glabra*as Possible Inhibitor of SARS-COV-2 Spike Glycoprotein and Non-Structural Protein-15: A Pharmacoinformatics Study. *J. Biomol. Struct. Dyn.* **2020**, *39*, 4686–4700. https://doi.org/10.1080/07391102.2020.1779132.
52. Salentin, S.; Haupt, V. J.; Daminelli, S.; Schroeder, M. Polypharmacology Rescored: Protein–Ligand Interaction Profiles for Remote Binding Site Similarity Assessment. *Prog. Biophys. Mol. Biol.* **2014**, *116*, 174–186. https://doi.org/10.1016/j.pbiomolbio.2014.05.006.
53. Chen, D.; Oezguen, N.; Urvil, P.; Ferguson, C.; Dann, S. M.; Savidge, T. C. Regulation of Protein-Ligand Binding Affinity by Hydrogen Bond Pairing. *Sci. Adv.* **2016**, *2*. https://doi.org/10.1126/sciadv.1501240.
54. Singh, R.; Bhardwaj, V. K.; Das, P.; Purohit, R. A Computational Approach for Rational Discovery of Inhibitors for Non-Structural Protein 1 of SARS-COV-2. *Comput. Biol. Med.* **2021**, *135*, 104555. https://doi.org/10.1016/j.compbiomed.2021.104555.
55. Poli, G.; Granchi, C.; Rizzolio, F.; Tuccinardi, T. Application of MM-PBSA Methods in Virtual Screening. *Molecules* **2020**, *25*, 1971. https://doi.org/10.3390/molecules25081971.

Supplementary materials

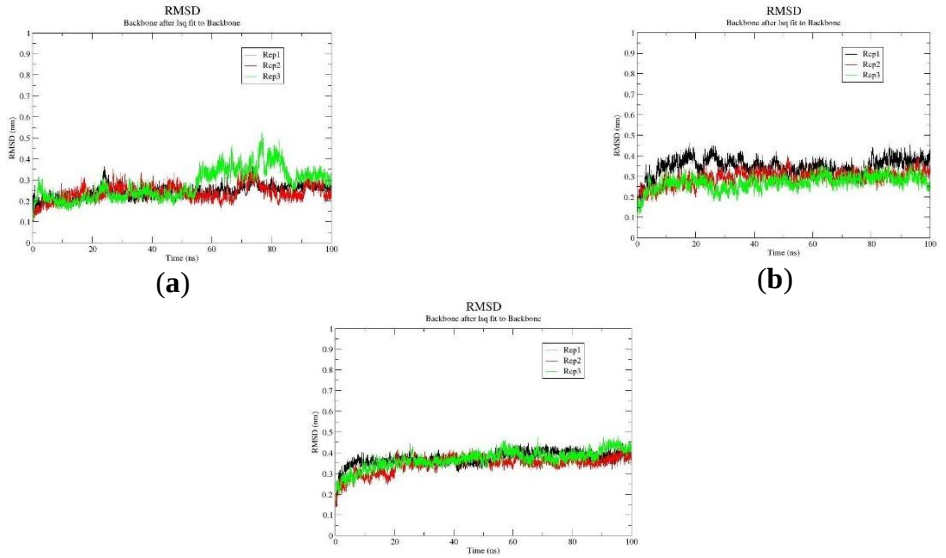

(**a**) (**b**)

(**c**)

Figure S1. Replicated RMSD plots of the complexes (a) 6LU7-Chromone-142, (b) 6M0J-Chromone-129, (c) 7ORB-Chromone-132.

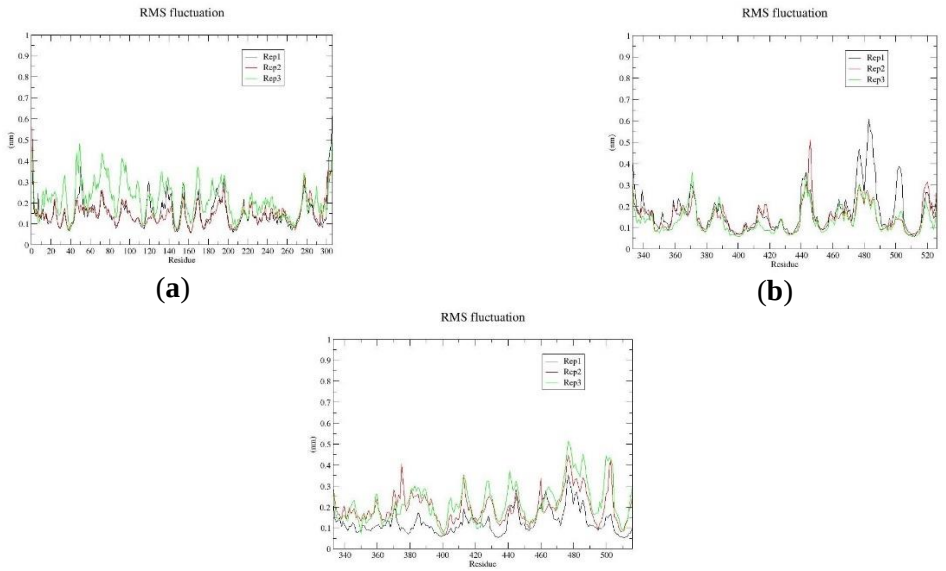

(**a**) (**b**)

(**c**)

Figure S2. Replicated RMSF plots of the complexes (a) 6LU7-Chromone-142, (b) 6M0J-Chromone-129, (c) 7ORB-Chromone-132

(**a**) (**b**)

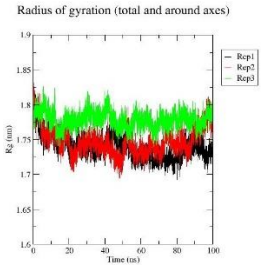

(**c**)

Figure S3. Replicated Rg plots of the complexes (a) 6LU7-Chromone-142, (b) 6M0J-Chromone-129, (c) 7ORB-Chromone-132.

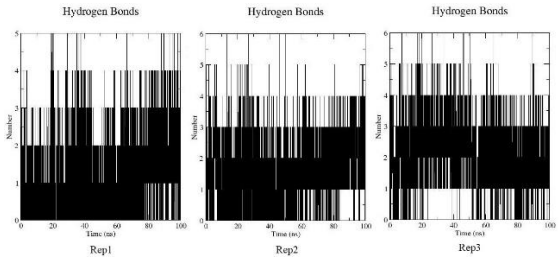

(a)

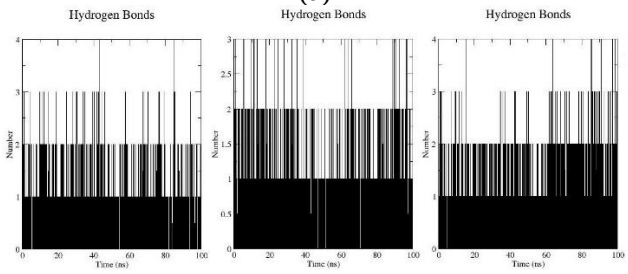

(b)

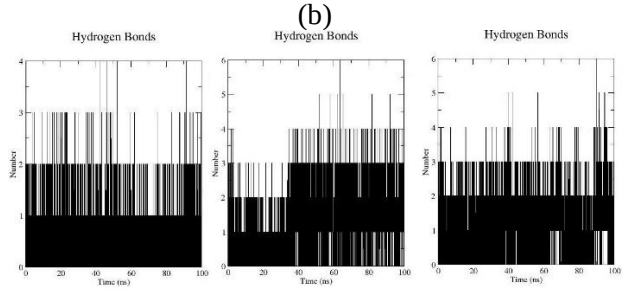

(**c**)

Figure S4. Replicated hydrogen bond plots of the complexes (a) 6LU7-Chromone-142, (b) 6M0J-Chromone-129, (c) 7ORB-Chromone-132.

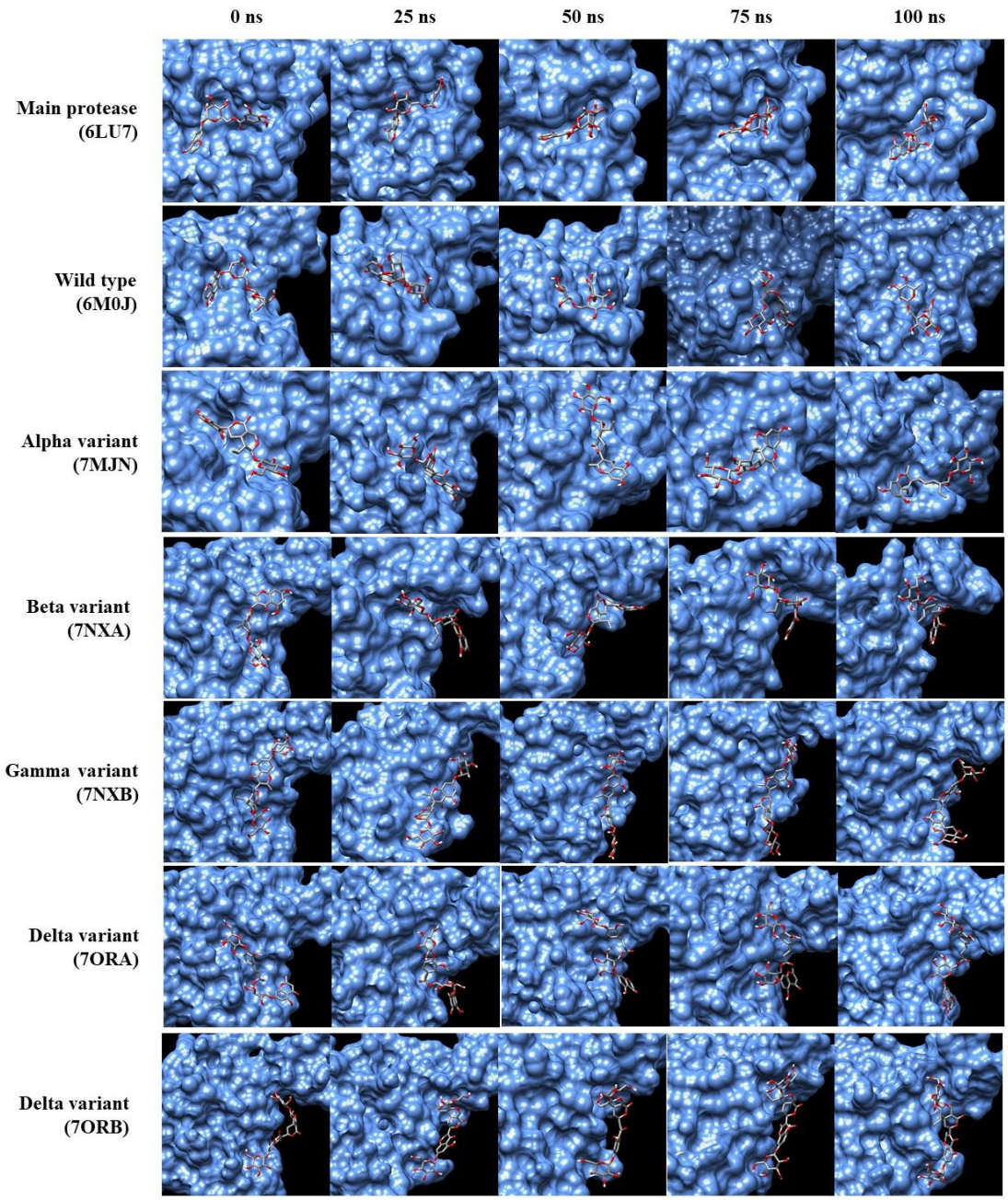

Figure S5. Frames from MD simulation of chromones with M^{pro} and spike RBDs of SARS-CoV-2 obtained at 0, 25, 50, 75, and 100 ns.

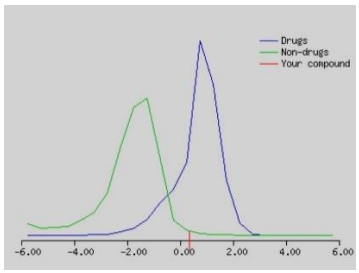

(a)

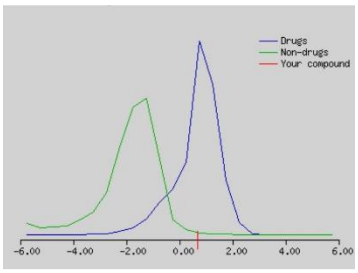

(b)

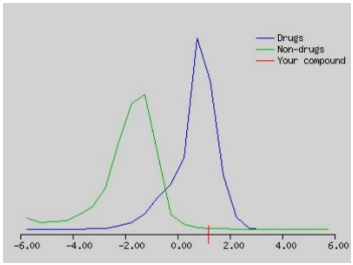

(c)

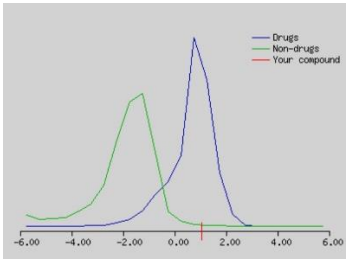

(d)

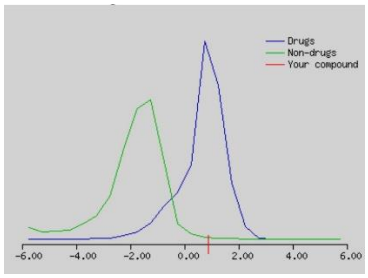

(**e**)

Figure S6. The graphical representation of the overall drug-likeness score of (a) Chromone-124, (b) Chromone-129, (c) Chromone-131, (d) Chromone-132, (e) Chromone-142 using the tool, Molsoft.

Table S1. Binding energy, mode of interaction, and interacting residues of SARS-CoV-2 M^{pro} with chromone.

Complex	Binding energy (kcal/mol)	Mode of interaction	Interacting residues	Distance (Å)
6LU7 - Chromone-142	-9.1	1. Hydrophobic interactions	THR25	3.91
			MET165	3.60
			GLN189	3.59
		2. Hydrogen bonds	THR26	2.04
			THR26	2.90
			GLY143	2.43
			SER144	3.13
			CYS145	2.48
			GLU166	2.53
			THR190	2.95
			THR190	2.15
			GLN192	2.89

Table S2. Binding energy, mode of interaction, and interacting residues of SARS-CoV-2 spike RBDs with chromones and residues common with RBD-ACE-2 complex.

Complex	Binding energy (kcal/mol)	Mode of interaction	Interacting residues of RBD	Distance (Å)	Residues common with RBD-ACE-2 complex
6M0J - Chromone-129	-7.8	1. Hydrophobic interactions	ASP405	3.80	LYS417
			GLU406	3.87	TYR453
			TYR505	3.69	GLY496
		2. Hydrogen bonds	ARG403	2.22	TYR505
			ARG403	2.10	
			ARG403	3.40	
			GLU406	2.43	
			LYS417	2.84	
			LYS417	3.37	
			TYR453	3.00	
			SER494	2.83	
			TYR495	2.79	
			TYR495	2.72	
			GLY496	2.31	
			GLY496	2.50	
			TYR505	2.41	
		3. π- stacking (Stacking type - T)	TYR505	5.13	
		4. π-Cation interactions	ARG403	4.62	
		5. Salt bridges	ARG403	4.57	
			ARG403	3.59	

Complex	Binding energy (kcal/mol)	Mode of interaction	Interacting residues of RBD	Distance (Å)	Residues common with RBD-ACE-2 complex
7MJN – Chromone-131	-8.1	1. Hydrophobic interaction	LYS417	3.65	ARG403 LYS417
		2. Hydrogen bonds	ARG403	2.92	GLN493
			LYS417	2.61	GLN498
			GLN493	2.61	TYR501
			SER494	2.03	
			GLY496	2.82	
			GLN498	3.15	
			TYR501	3.40	
		3. π-Cation interactions	LYS417	4.38	
7NXA – Chromone-131	-7.3	1. Hydrophobic interactions	ILE418	3.52	TYR453
			TYR453	3.36	LEU455
			LEU455	3.80	PHE456
			PHE456	3.99	TYR489
			TYR495	3.55	SER494
		2. Hydrogen bonds	TYR453	2.17	
			TYR489	2.88	
			TYR489	2.75	
			SER494	2.19	
			GLY496	2.37	
			GLY496	3.19	
		3. Salt bridges	ARG403	3.59	
			ARG403	3.84	
7NXB – Chromone-132	-7.4	1. Hydrophobic interaction	PHE456	3.51	TYR453 PHE456
		2. Hydrogen bonds	TYR453	2.53	TYR489
			TYR473	2.21	TYR505
			TYR489	2.46	
			TYR505	2.56	
		3. Salt bridges	ARG403	4.51	
			ARG403	3.82	
7ORA – Chromone-124	-7.8	1. Hydrophobic interaction	TYR495	3.74	LYS417 TYR449
		2. Hydrogen bonds	ARG403	2.22	GLY496
			ARG403	3.30	GLN498
			ARG403	2.52	ASN501
			GLU406	2.54	
			LYS417	2.93	
			TYR449	2.50	
			GLY496	1.83	
			GLN498	2.93	
			ASN501	2.75	
		3. π-Cation interactions	ARG403	3.88	
		4. Salt bridges	LYS417	3.53	
7ORB – Chromone-132	-7.1	1. Hydrophobic interaction	TYR449	3.57	TYR449 GLN493
		2. Hydrogen bonds	GLY485	3.13	GLY496
			PHE490	3.37	ASN501
			PHE490	1.92	
			GLN493	2.66	
			GLY496	2.16	
			ASN501	2.31	
			ASN501	2.39	

Table S3. Mode of binding and interacting residues of the SARS-CoV-2 Mpro and S-RBDs with chromones at the end of 100 ns in PRODRG-derived topology file.

Complex	Mode of interaction	Interacting residues	Distance (Å)
6LU7 - Chromone-142	1. Hydrophobic interactions	TYR54	3.38
	2. Hydrogen bonds		
		ARG40	2.52
		SER46	3.60
		TYR54	2.52

Complex	Mode of interaction	Interacting residues	Distance (Å)
		GLU166	2.46
		GLU166	3.23
		GLU166	3.30
	3. π-Stacking	VAL186	3.02
	4. Salt bridge	GLN192	3.54
		HIS41	4.13
		HIS41	3.51
6M0J - Chromone-129	1. Hydrophobic interactions	TYR449	3.45
		TYR505	3.48
	2. Hydrogen bonds	ARG403	2.41
		GLY447	3.66
		GLN498	2.89
		VAL503	3.35
7MJN – Chromone-131	1. Hydrophobic interaction	TYR449	3.50
		TYR505	3.92
	2. Hydrogen bonds	ARG403	2.57
		SER494	3.27
		SER494	3.07
		GLY496	2.76
		TYR501	2.62
		TYR501	2.68
	3. Salt bridge	ARG403	3.41
7NXA – Chromone-131	1. Hydrophobic interactions	PHE456	3.67
		TYR473	3.93
	2. Hydrogen bonds	PHE456	2.41
		ARG457	3.20
		GLY476	3.43
		PHE490	3.54
		LEU492	2.84
7NXB – Chromone-132	1. Hydrophobic interaction	TYR449	3.75
		GLN493	3.67
		TYR505	3.79
		TYR505	3.71
	2. Hydrogen bonds	TYR449	2.43
		PHE490	3.47
		LEU492	3.24
		SER494	3.25
	3. Salt bridges	ARG403	4.41
7ORA – Chromone-124	1. Hydrophobic interaction	TYR449	3.94
		TYR489	3.51
	2. Hydrogen bonds	ARG403	3.63
		ARG403	3.67
		LEU455	2.53
		SER494	3.17
		GLY496	3.31
7ORB – Chromone-132	1. Hydrophobic interaction	LEU455	3.23
		TYR473	3.80
		TYR473	3.98
		TYR489	3.85
		PHE490	3.70
		GLN493	3.92
	2. Hydrogen bonds	ASN448	3.71
		TYR489	3.13
		TYR495	3.18

Table S4. Calculated energy components and net MM-PBSA free energy (kJ/mol) values for all the docked complexes from 100 ns MD simulation trajectories.

Energy components	Van der Waals energy	Electrostatic energy	Polar solvation energy	SASA energy	Binding energy
6LU7-Chromone-142	-221.328 ± 13.903	-31.439 ± 7.348	107.759 ± 11.903	-19.793 ± 1.252	-164.801 ± 11.619
6M0J-Chromone-129	-110.899 ± 14.167	-2.168 ± 3.387	37.105 ± 12.269	-11.269 ± 1.859	-87.232 ± 16.098
7MJN-Chromone-131	-132.958 ± 14.191	-33.109 ± 10.890	87.091 ± 23.982	-13.841 ± 1.852	-92.815 ± 23.718
7NXA-Chromone-131	-169.221 ± 11.426	-6.196 ± 4.826	71.973 ± 10.043	-17.516 ± 1.295	-120.960 ± 11.277
7NXB-Chromone-132	-173.257 ± 12.555	-19.395 ± 6.160	85.295 ± 11.791	-18.865 ± 1.265	-126.223 ± 14.693
7ORA-Chromone-124	-219.977 ± 11.705	0.613 ± 8.465	66.134 ± 9.822	-22.187 ± 1.285	-175.418 ± 12.453
7ORB-Chromone-132	-185.400 ± 13.327	1.499 ± 5.592	78.912 ± 11.484	-20.250 ± 1.415	-125.240 ± 15.24

Table S5. The binding free energy of docked complexes from different replications.

Complexes	Replicate 1 (kJ/mol)	Replicate 2 (kJ/mol)	Replicate 3 (kJ/mol)
6LU7-Chromone-142	-179.609 ± 12.772	-164.801 ± 11.619	-152.142 ± 19.381
6M0J-Chromone-129	-87.232 ± 16.098	-83.350 ± 23.859	-116.081 ± 11.126
7ORB-Chromone-132	-125.240 ± 15.246	-125.537 ± 33.085	-121.938 ± 11.514

Table S6. Natural chromones used for the present study as in the literature (Semwal *et al*. 2020). (Reference cited in the main manuscript).

Name	Plant source	Structure	Name in the manuscript
Conyzorigun	*Ageratum Conyzoides*	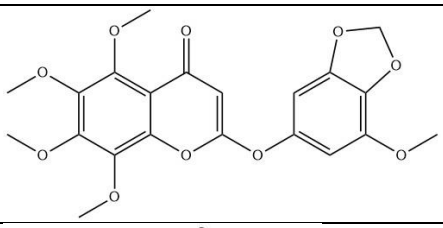	Chromone-1
2-Isopropyl-C6-methoxy chromone	*Alangium Salvifolium*	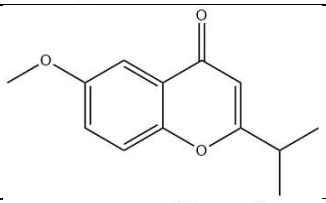	Chromone-2
Hamaudol	*Angelica genuflexa*	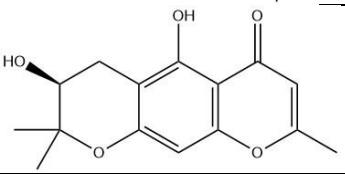	Chromone-3
Cimifugin	*Angelica genuflexa*	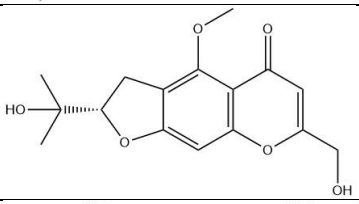	Chromone-4
Sec-O-glucosylhamaudol	*Angelica genuflexa*	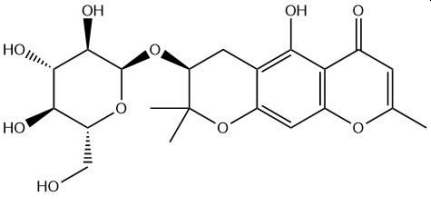	Chromone-5

Name	Plant source	Structure	Name in the manuscript
Prim-O glucosylcimifugin	*Angelica genuflexa*	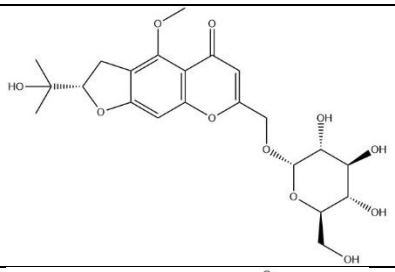	Chromone-6
Isoaloeresin D	*Aloe vera*	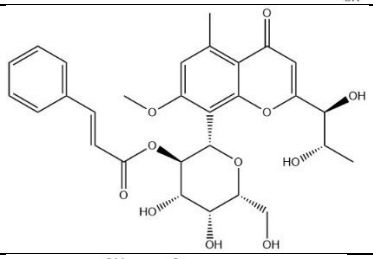	Chromone-7
5-hydroxy-6-methoxy-2-(2-phenylethyl)chromone	*Aquilaria sinensis*	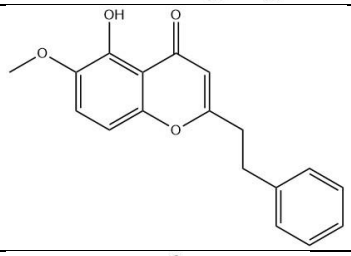	Chromone-8
6-hydroxy-2-(2-hydroxy-2-phenylethyl)	*Aquilaria sinensis*	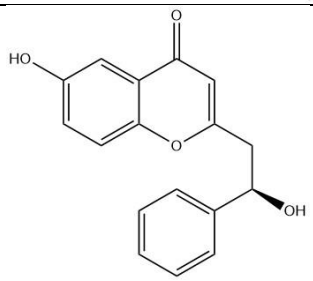	Chromone-9
4’-O-glucosyl-isoaloeresin DI	*Aloe vera*	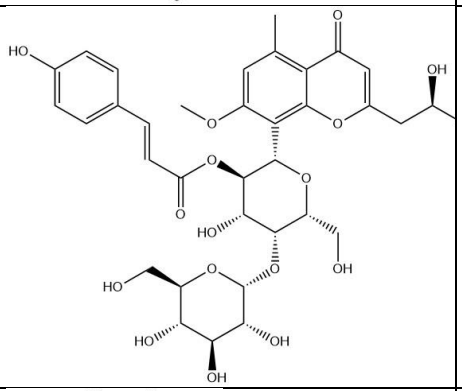	Chromone-10
8-C-glucosyl-noreugenin	*Aloe vera*	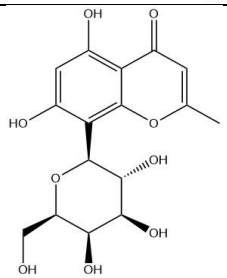	Chromone-11

Name	Plant source	Structure	Name in the manuscript
7-O-methylaloesin	*Aloe rupestris*	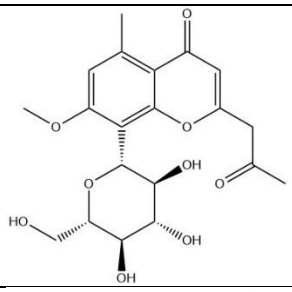	Chromone-12
Rabaichromone	*Aloe rabaiensis*	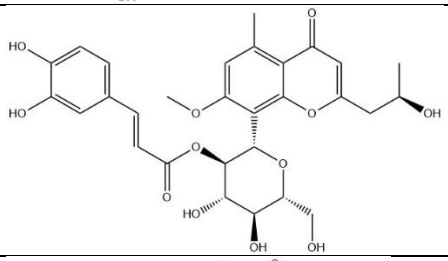	Chromone-13
Aloeresin D	*Aloe rabaiensis*	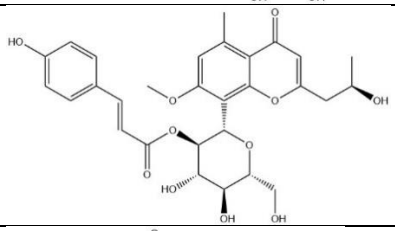	Chromone-14
Qinanones G	*Aquilaria sinensis*	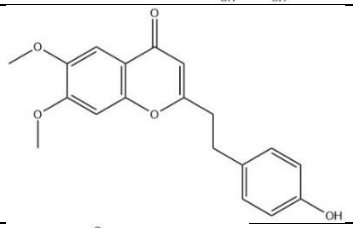	Chromone-15
2-(2-Phenylethyl)chromone	*Aquilaria sinensis*	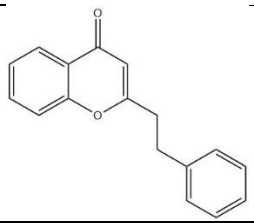	Chromone-16
5,8-dihydroxy-2-(2-p-methoxyphenylethyl) chromone	*Aquilaria sinensis*	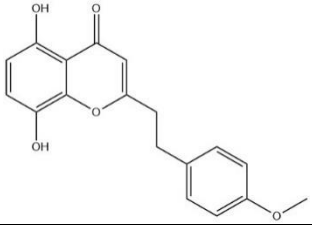	Chromone-17
5,8-dihydroxy-2-(2-phenylethyl)-chromone	*Aquilaria sinensis*	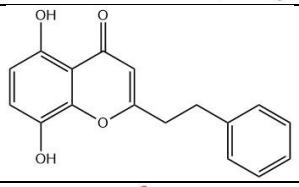	Chromone-18
6-hydroxy-2-[2-(4'-methoxylphenyl)ethyl]chromone	*Aquilaria sinensis*	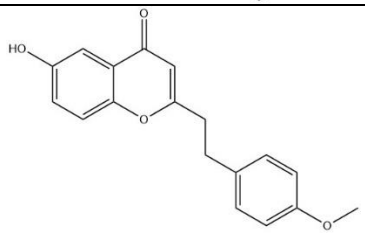	Chromone-19

Name	Plant source	Structure	Name in the manuscript
6-methoxy-2-(2-phenylethyl)chromone	*Aquilaria sinensis*	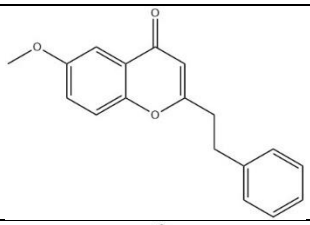	Chromone-20
6,7-dimethoxy-2-(2-phenylethyl) chromone	*Aquilaria sinensis*	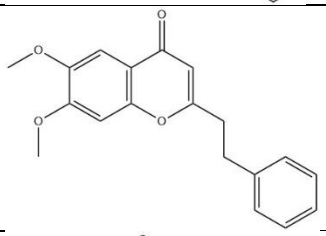	Chromone-21
6-methoxy-2[2-(3'-methoxyphenyl) ethyl]chromone	*Aquilaria sinensis*	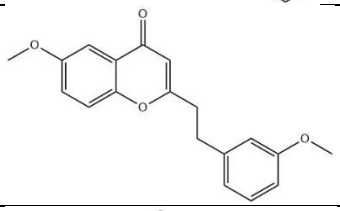	Chromone-22
6-hydroxy-2-(2-phenylethyl)chromone	*Aquilaria sinensis*	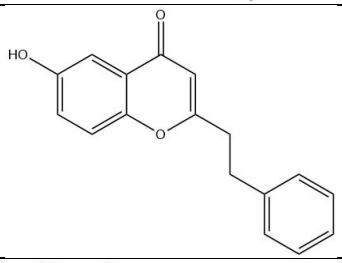	Chromone-23
5-hydroxy-8-methoxy-2-[2-(4'methoxyphenyl)-ethyl]chromone	*Aquilaria sinensis*	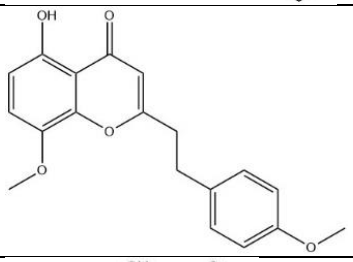	Chromone-24
5-Hydroxy-7-methoxychromone	*Artemisia campestris* subsp. *Maritima*	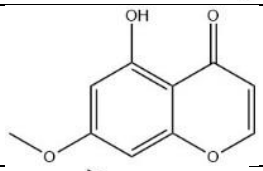	Chromone-25
5,7-dimethoxychromone	*Artemisia campestris* subsp. *Maritima*	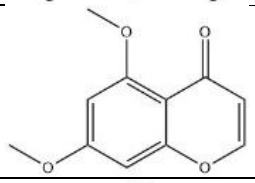	Chromone-26
6-β-C-Glucopyranosyl-5,7 dihydroxy-2-Isopropylchromone	*Baeckea frutescens*	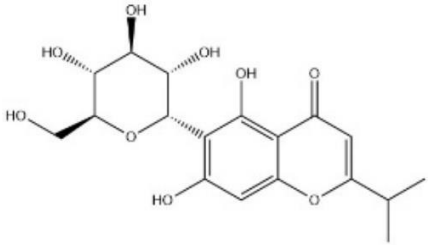	Chromone-27

Name	Plant source	Structure	Name in the manuscript
8-β-C-Glucopyranosyl-5,7-dihydroxy-2-Isopropylchromone	*Baeckea frutescens*	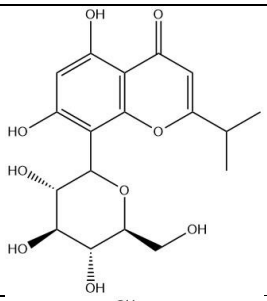	Chromone-28
6-β-C-Glucopyranosyl-5,7-dihydroxy-2-Methylchromone	*Baeckea frutescens*	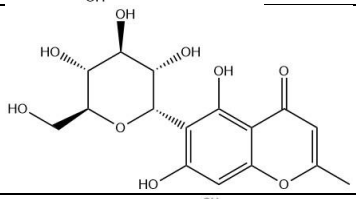	Chromone-29
6-β-C-(2'-Galloylglucopyranosyl)-5,7-dihydroxy-2-Isopropylchromone	*Baeckea frutescens*	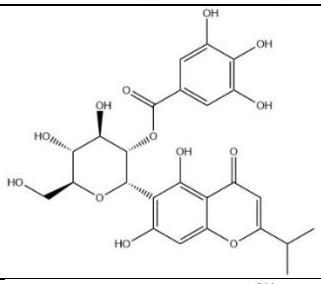	Chromone-30
8-b;-C-(2'-Galloylglucopyranosyl)-5,7-dihydroxy-2-Isopropylchromone	*Baeckea frutescens*	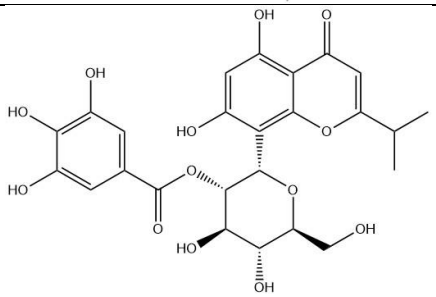	Chromone-31
5-hydroxy-7-(2'-hydroxypropyl)-2-methyl-chromone	*Berchemia lineata*	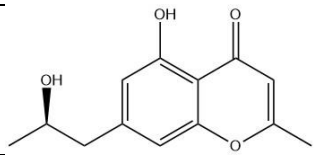	Chromone-32
(-)-(1'R, 2'S)-erythro-5-hydroxy-7-(1',2'-dihydroxypropyl)-2-methyl-chromone	*Berchemia lineata*	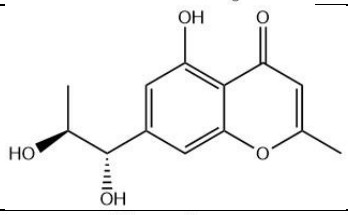	Chromone-33
5-Hydroxy-6-methoxy-2-[2-(2-hydroxyphenyl)-ethyl]-Chromone	*Bothriochloa ischaemum*	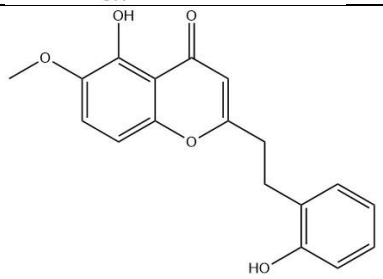	Chromone-34

Name	Plant source	Structure	Name in the manuscript
5-hydroxy-2-[2-(2-hydroxyphenyl)-ethyl]-Chromone	*Bothriochloa ischaemum*	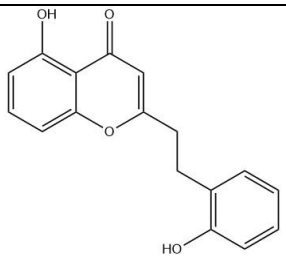	Chromone-35
Saikochromoside A	*Bupleurum chinense*	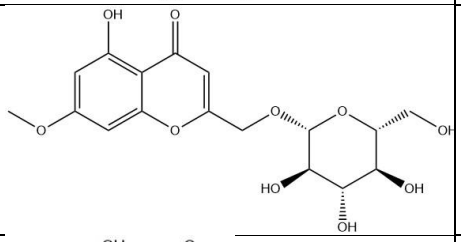	Chromone-36
5,7-dihydroxychromone	*Calluna vulgaris*	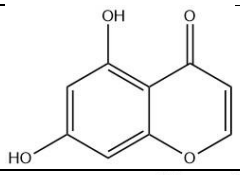	Chromone-37
5,7-dihydroxychromone 7-β-D-glucoside	*Calluna vulgaris*	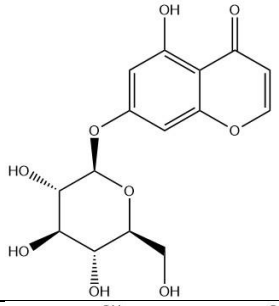	Chromone-38
Aloeresin E	*Aloe peglerae*	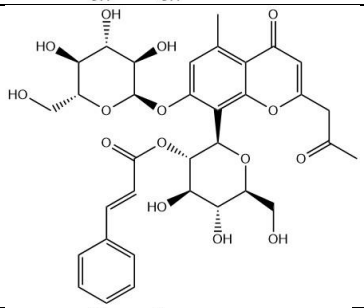	Chromone-39
2-Carboxyethenyl-5,7-dihydroxychromone	*Aloe jacksonii*	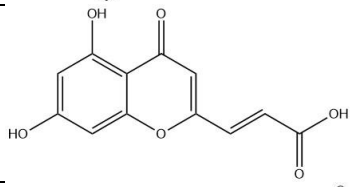	Chromone-40
2′-O-[p-Methoxy-(E)-cinnamoyl]-(S)-aloesinol	*Aloe nobilis*	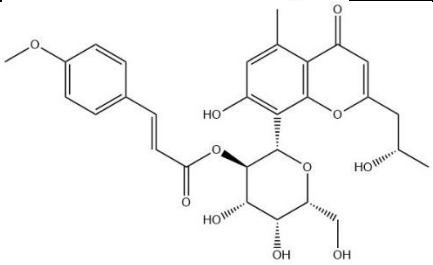	Chromone-41

Name	Plant source	Structure	Name in the manuscript
2′-O-Coumaroyl-(S)-aloesinol	*Aloe nobilis*	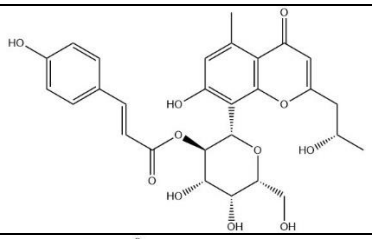	Chromone-42
C-2′-Decoumaroyl-aloeresin G	*Aloe nobilis*	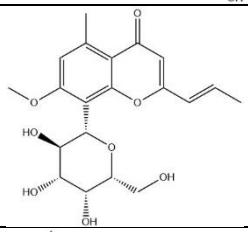	Chromone-43
5-acetonyl-7-hydroxy-2-Methylchromone	*Cassia multijuga*	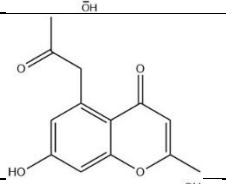	Chromone-44
5,40-dihydroxy-7-methyl 3-benzyl chromone	*Cassia nodosa*	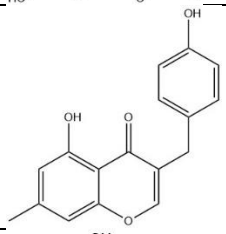	Chromone-45
Acetonyl-6-glycosyl-7-hydroxy-2-methylchromone-7-O-β-D Glucopyranoside	*Cassia multijuga*	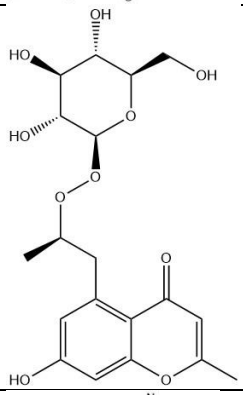	Chromone-46
Cassiadinine	*Cassia siamea*	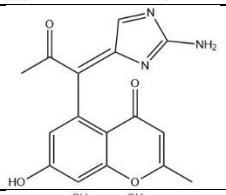	Chromone-47
2-Acetonyl-5-methyl-7-hydroxy-6-C-glucopyranosyl chromone-2”-O-glucopyranoside	*Chrozophora prostrata*	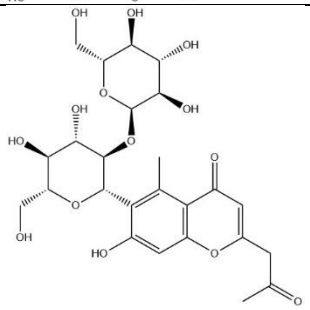	Chromone-48

Name	Plant source	Structure	Name in the manuscript
Chrysograyanon	*Chrysosplenium grayanum*	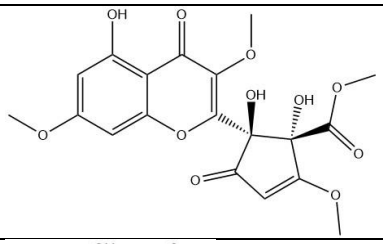	Chromone-49
5,7-Dihydroxy-8-methoxychromone	*Citrus reticulata*	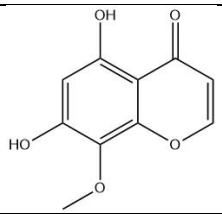	Chromone-50
5,7-Dihydroxy-2-(n-heptaeicosanyl)chromone	*Clusia nemorosa*	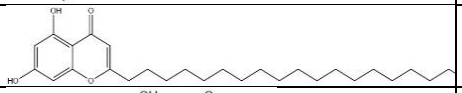	Chromone-51
3,3-dimethylallylspatheliachromene	*Cneorum tricoccum*	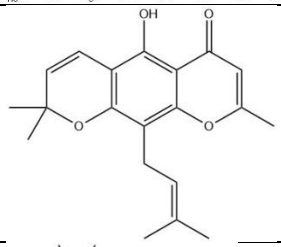	Chromone-52
Spatheliabischromene	*Cneorum tricoccum*	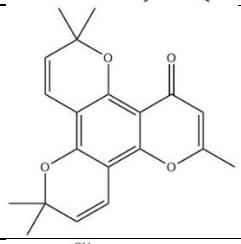	Chromone-53
Cnidimosides A	*Cnidium japonicum*	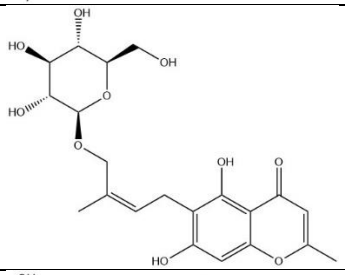	Chromone-54
Cnidimosides B	*Cnidium japonicum*	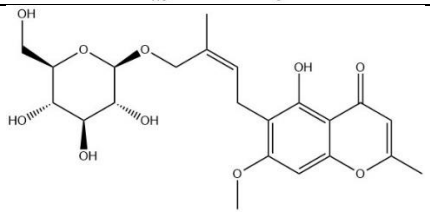	Chromone-55
Cnidimol A	*Cnidium monnieri*	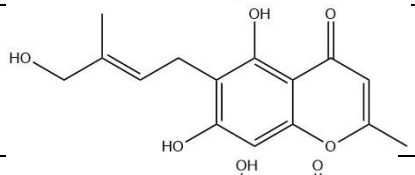	Chromone-56
Cnidimol B	*Cnidium monnieri*	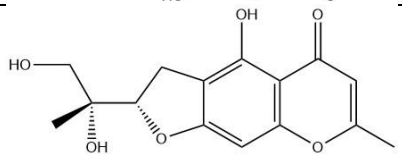	Chromone-57

Name	Plant source	Structure	Name in the manuscript
Karenin	*Cnidium monnieri*	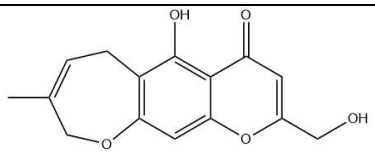	Chromone-58
Cnidimol C	*Cnidium monnieri*	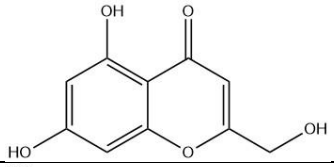	Chromone-59
Cnidimol D	*Cnidium monnieri*	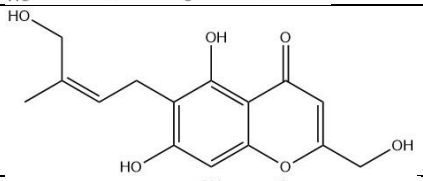	Chromone-60
Cnidimol E	*Cnidium monnieri*	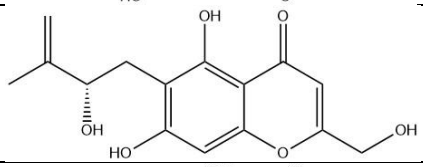	Chromone-61
Cnidimol F	*Cnidium monnieri*	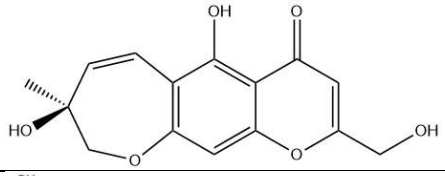	Chromone-62
Hydroxycindimoside A	*Cnidium monnieri*	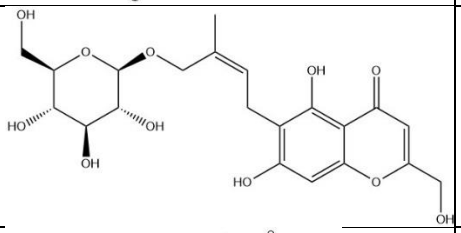	Chromone-63
7-o-methylaloeresin a	*Commzphora socotrana*	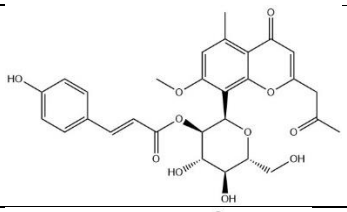	Chromone-64
Aloeresin A	*Commzphora socotrana*	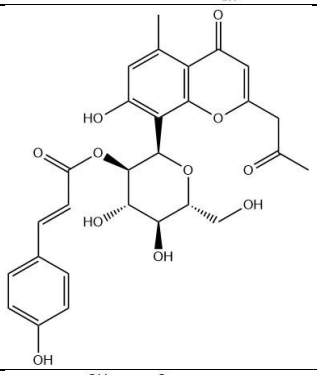	Chromone-65
5,7-dihydroxy-2-[2-(4-hydroxyphenyl)-ethyl]-chromone	*Cucumis melo var. Reticulatus*	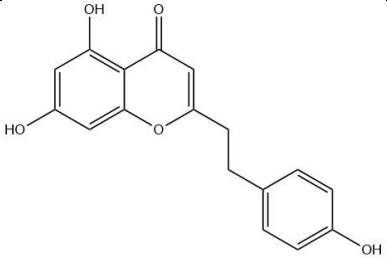	Chromone-66

Name	Plant source	Structure	Name in the manuscript
5,7-dihydroxy-2-[2-(3,4-dihydroxyphenyl) ethyl] Chromone	*Cucumis melo var. Reticulatus*	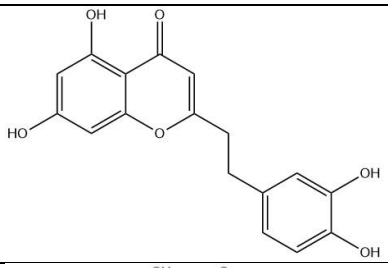	Chromone-67
7-glucosyloxy-5-hydroxy-2-[2-(4-hydroxyphenyl)ethyl]chromone	*Cucumis melo var. Reticulatus*	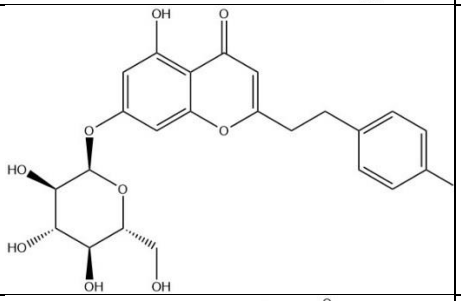	Chromone-68
8-C-Glucosyl-7-methoxy-(R)-aloesol	*Aloe Vera*	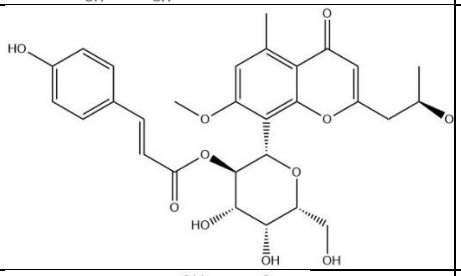	Chromone-69
5,7-dihydroxychromone-7 -o-β- D-glucuronide methyl ester	*Davallia mariesii*	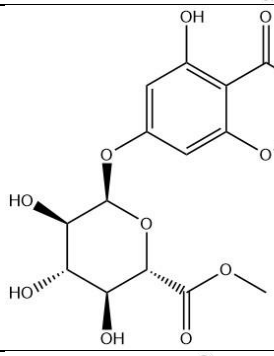	Chromone-70
Dennettine	*Dennettia tripetala*	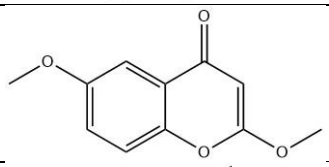	Chromone-71
6-(3-methylbut-2-enyl) allopteroxylin methyl ether	*Dictyoloma vandellianum*	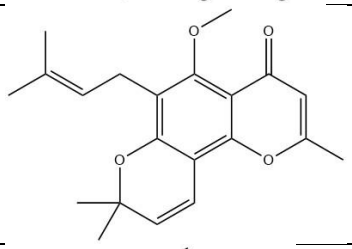	Chromone-72
3,3-dimethylallylspatheliachromene Methyl ether	*Dictyoloma vandellianum*	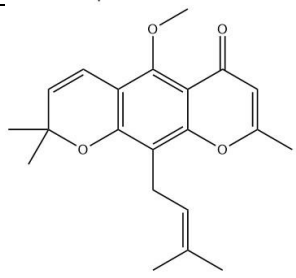	Chromone-73

Name	Plant source	Structure	Name in the manuscript
5-O-methylcneorumchrom	*Dictyoloma vandellianum*	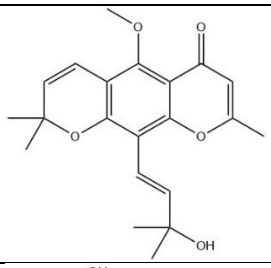	Chromone-74
(2'S)-2'-hydroxy-7-O-methylallopeucenin 2'-O-β-D-glucopyranoside	*Diplolophium buchananii*	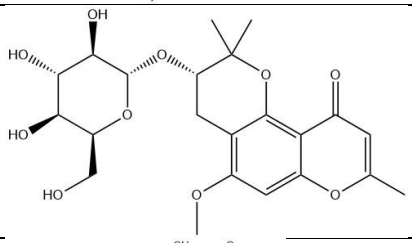	Chromone-75
Drynachromosides C	*Drynaria fortunei*	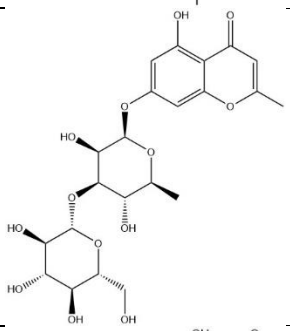	Chromone-76
Drynachromosides D	*Drynaria fortunei*	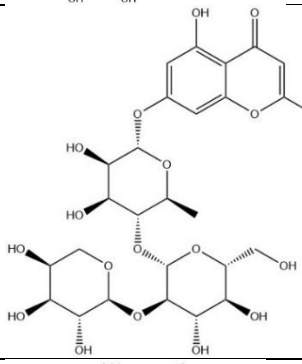	Chromone-77
5,7-dihydroxy-2-Methyl chromone	*Drynaria fortunei*	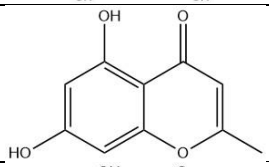	Chromone-78
5,7-dihydroxy-2-hydroxymethyl chromone	*Drynaria fortunei*	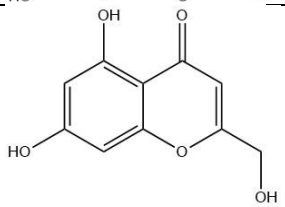	Chromone-79
Schumanniofioside A	*Drynaria fortunei*	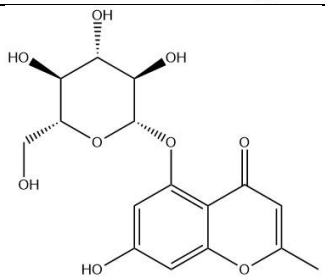	Chromone-80

Name	Plant source	Structure	Name in the manuscript
5-hydroxy-2-methylchromone-7-O-rutinoside	*Drynaria fortunei*	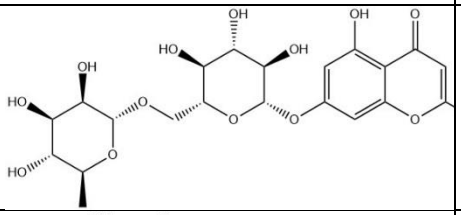	Chromone-81
Drynachromoside B	*Drynaria fortunei*	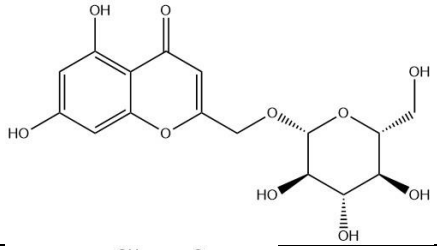	Chromone-82
Stellatin	*Dysophylla stellata*	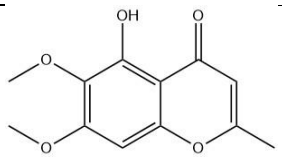	Chromone-83
Chrotacumines A	*Dysoxylum acutangulum*	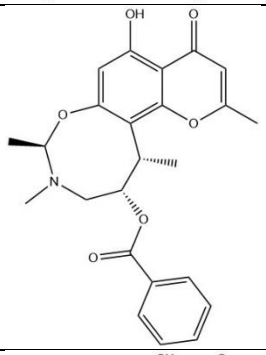	Chromone-84
Chrotacumines B	*Dysoxylum acutangulum*	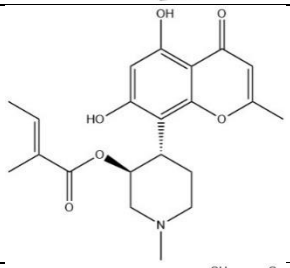	Chromone-85
Chrotacumines C	*Dysoxylum acutangulum*	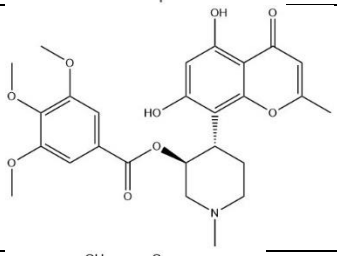	Chromone-86
Chrotacumines D	*Dysoxylum acutangulum*	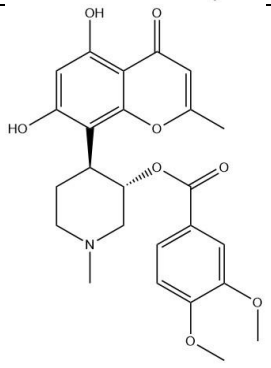	Chromone-87

Name	Plant source	Structure	Name in the manuscript
Rohitukine	*Dysoxylum acutangulum*	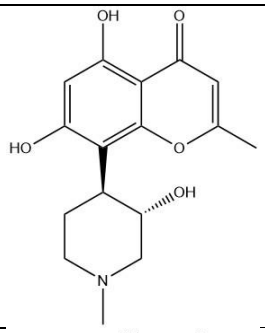	Chromone-88
Chrotacumines E	*Dysoxylum acutangulum*	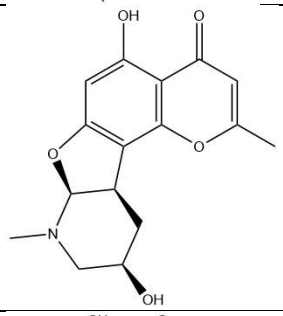	Chromone-89
Chrotacumines F	*Dysoxylum acutangulum*	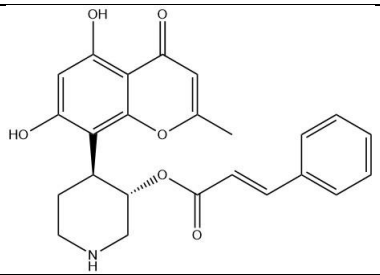	Chromone-90
Chrotacumines G	*Dysoxylum acutangulum*	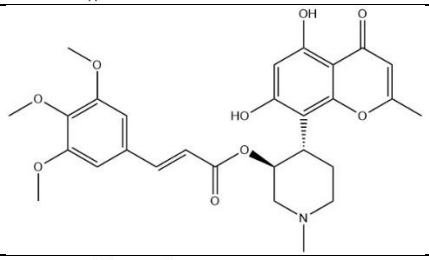	Chromone-91
Chrotacumines H	*Dysoxylum acutangulum*	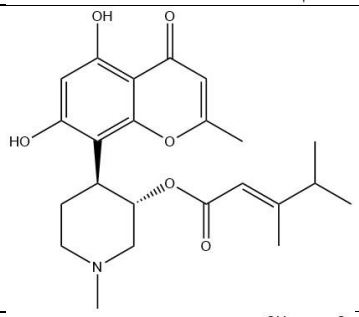	Chromone-92
Chrotacumines I	*Dysoxylum acutangulum*	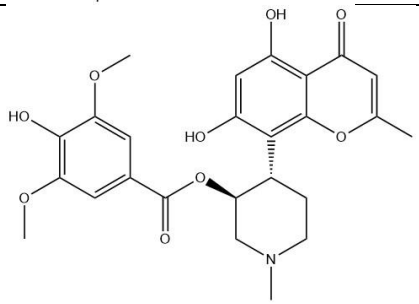	Chromone-93

Name	Plant source	Structure	Name in the manuscript
Chrotacumines J	*Dysoxylum acutangulum*	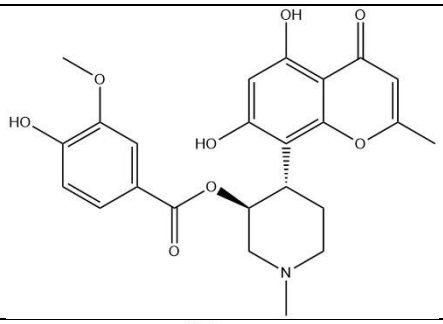	Chromone-94
Dysoline	*Dysoxylum binectariferum*	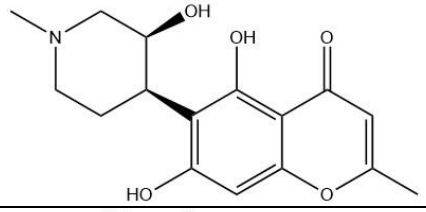	Chromone-95
Rohitukine	*Dysoxylum binectariferum*	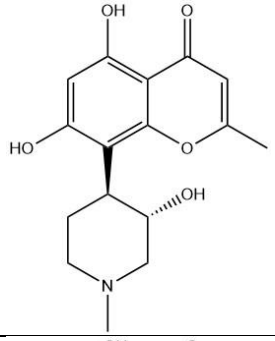	Chromone-96
Rohitukine N-oxide	*Dysoxylum binectariferum*	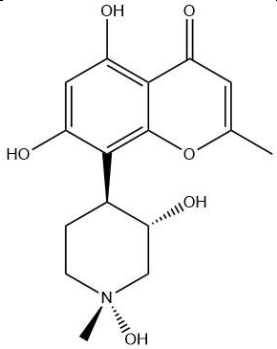	Chromone-97
Eucryphin	*Eucryphia cordifolia*	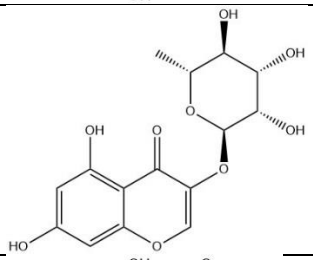	Chromone-98
Lsobiflorin	*Eugenia caryophyllata*	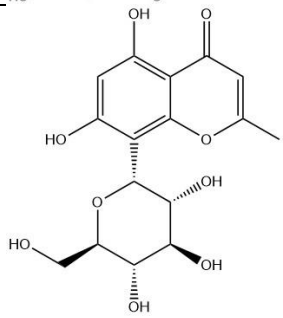	Chromone-99

Name	Plant source	Structure	Name in the manuscript
Biflorin	*Eugenia caryophyllata*	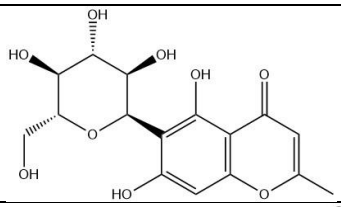	Chromone-100
7-O-methylaloeresin A	*Aloe marlothii*	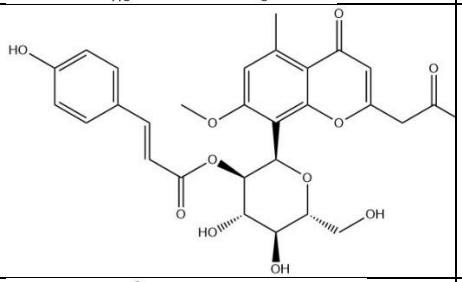	Chromone-101
Pallidones I	*Ferula pallida*	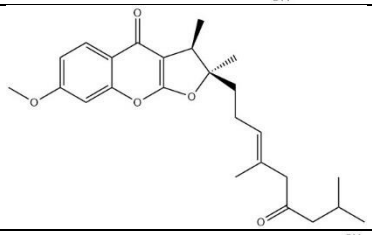	Chromone-102
Pallidones J	*Ferula pallida*	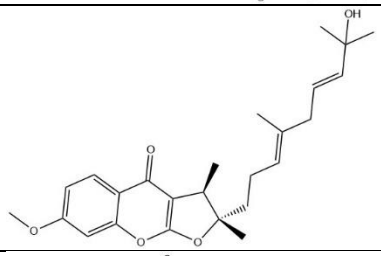	Chromone-103
Ferulin D	*Ferula ferulaeoides*	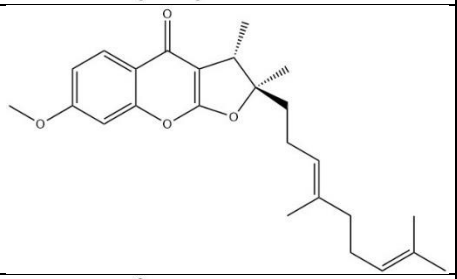	Chromone-104
Ferulin E	*Ferula ferulaeoides*	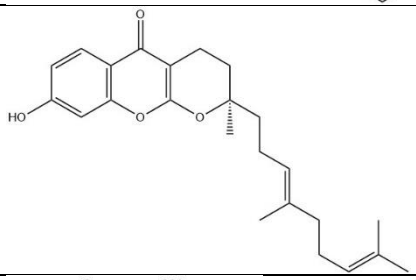	Chromone-105
5,6-dihydroxy-2-Methylchromone	*Ficus lyrata*	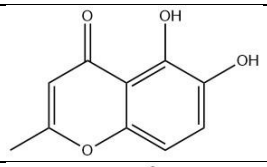	Chromone-106
2-propyl-7,8-(methylenedioxy)chromone	*Galipea granulosa*	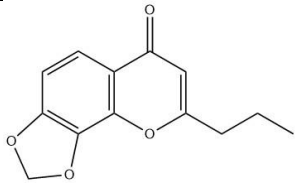	Chromone-107

Name	Plant source	Structure	Name in the manuscript
Aloeresin F	*Aloe peglerae*	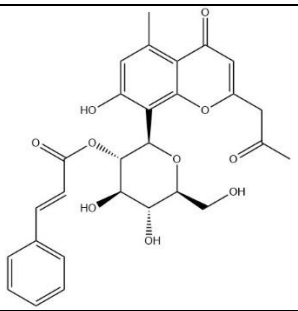	Chromone-108
Gerdelavin B	*Gerbera delavayi*	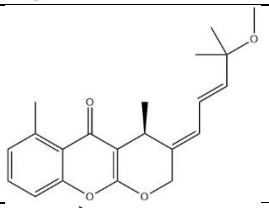	Chromone-109
2-hydroxymethylallopraeroxylin	*Harrisonia abyssinica*	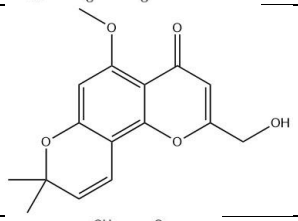	Chromone-110
5,7-dihydroxy-6,8-dimethoxy-2-methyl-H-4-chromen-4-one	*Hymenocallis littoralis*	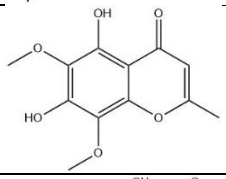	Chromone-111
Hyperimone A	*Hypericum erectum*	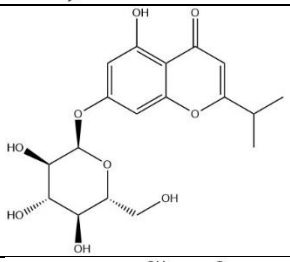	Chromone-112
Hyperimone B	*Hypericum erectum*	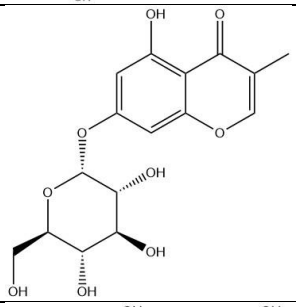	Chromone-113
Urachromone A	*Hypericum henryi* subsp. *Uraloides*	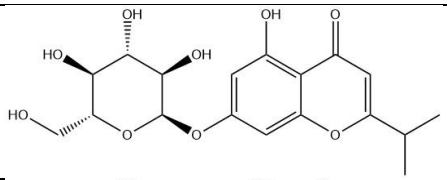	Chromone-114
Urachromone B	*Hypericum henryi* subsp. *Uraloides*	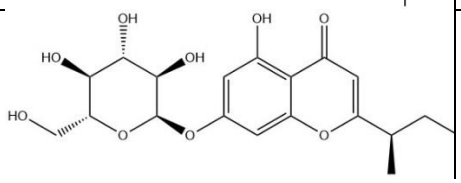	Chromone-115

Name	Plant source	Structure	Name in the manuscript
5,7-dihydroxy-2-(1-methylpropyl)chromone-8-β-D-glucoside	*Hypericum Japonicum*	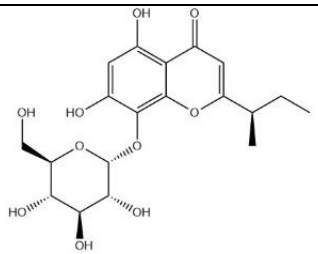	Chromone-116
5,7-dihydroxy-2-isopropyl chromone-8-β-D-glucoside	*Hypericum Japonicum*	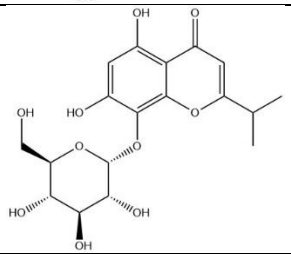	Chromone-117
5-Hydroxy-7-methoxy-3-methyl-chromen-4-one	*Hypericum perforatum*	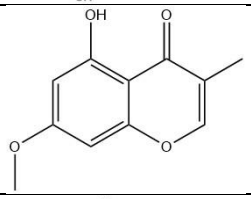	Chromone-118
8-hydroxy-2-(2-phenylethyl) Chromone	*Imperata cylindrica*	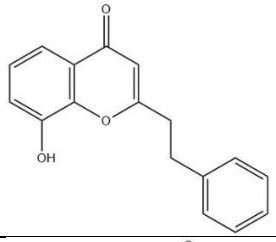	Chromone-119
2-(2-phenylethyl)chromone-8-O-β-D-gluco pyranoside	*Imperata cylindrica*	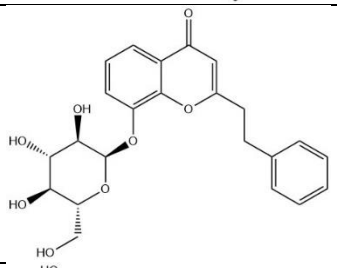	Chromone-120
Undulatoside A	*Knoxia corymbosa*	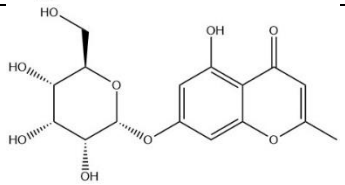	Chromone-121
Corymbosin K2	*Knoxia corymbosa*	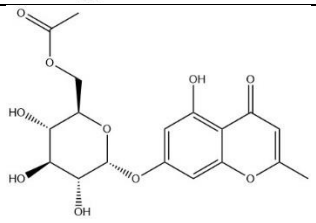	Chromone-122

Name	Plant source	Structure	Name in the manuscript
Corymbosin K3	*Knoxia corymbosa*	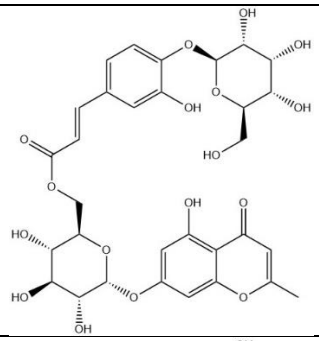	Chromone-123
7-O-[6-O-(4-O-trans-feruloyl-β-D-allopyranosyl)]-B-D-glucopyranosyl-5-hydroxy-2-methylchromone	*Knoxia corymbosa*	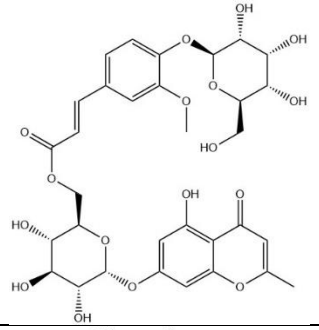	Chromone-124
Lathodoratin	*Lathyrus odoratus*	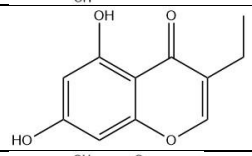	Chromone-125
Methyl-lathodoratin	*Lathyrus odoratus*	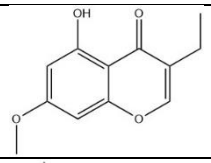	Chromone-126
2-methyl-5-hydroxy-6-[3-methyl-2-butenyl]-7-methoxychromone	*Lomatium macrocarpum*	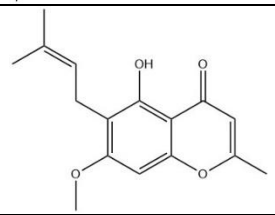	Chromone-127
Melachromone	*Melaleuca cajuputi*	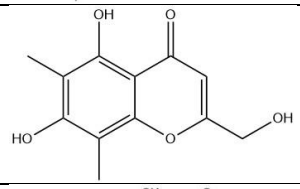	Chromone-128
5-Hydroxy-chromone-7-rutinoside	*Mentha longifolia*	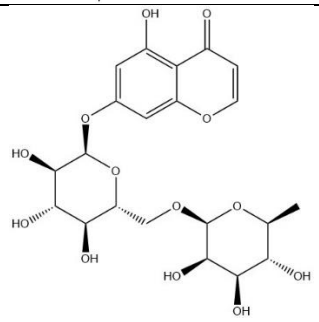	Chromone-129

Name	Plant source	Structure	Name in the manuscript
Pulverin	*Neochamaelea pulverulenta*	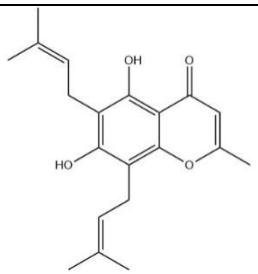	Chromone-130
Sessilifoside	*Neonauclea sessilifolia*	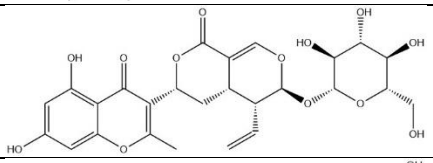	Chromone-131
7”-O-β-D-Glucopyranosylsessilifoside	*Neonauclea sessilifolia*	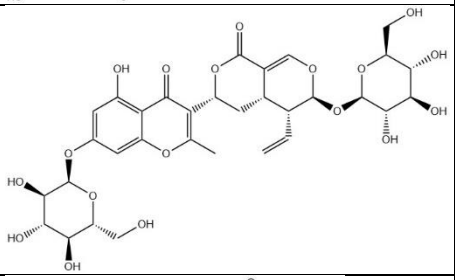	Chromone-132
Aloesin-2’-O-tigloyl ester	*Aloe jacksonii*	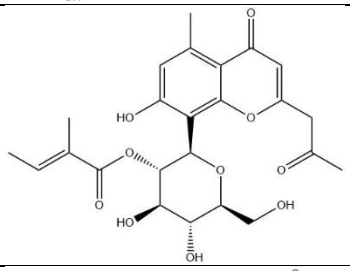	Chromone-133
Aloeresin B	*Aloe jacksonii*	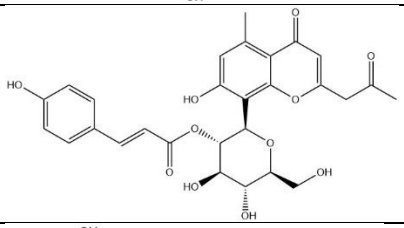	Chromone-134
11-hydroxy-sec-O-glucosylhamaudol	*Ostericum koreanum*	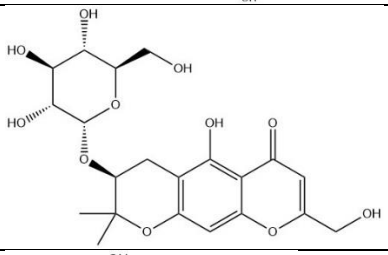	Chromone-135
2-methyl-5,7-dimethoxy-chromone-6-β-D-glucoside	*Pancratium biflorum*	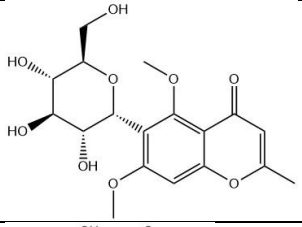	Chromone-136
2-methyl-5,6-dihydroxy-7-methoxychromone	*Pancratium biflorum*	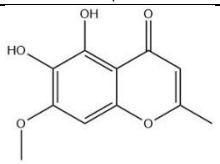	Chromone-137

Name	Plant source	Structure	Name in the manuscript
Maritimin	*Pancratium maritimum*	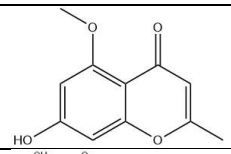	Chromone-138
Peperovulcanone A	*Peperomia vulcanica*	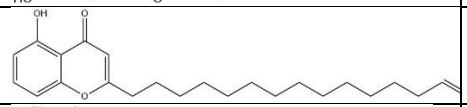	Chromone-139
Peperovulcanone B	*Peperomia vulcanica*	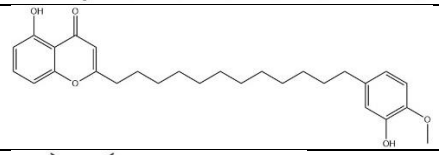	Chromone-140
Pilopleurin	*Pilopleura kozo-poljanskii*	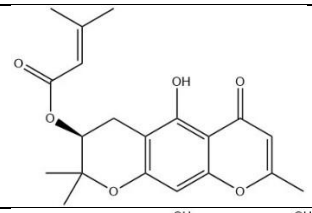	Chromone-141
7-O-(6′-galloyl)-β-D-glucopyranosyl-5-hydroxychromone	*Polygonum capitatum*	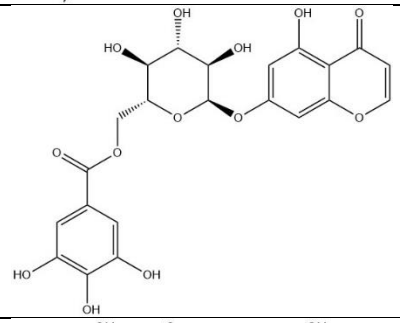	Chromone-142
3,5,7-trihydroxylchromone-3-O-α-L-arabinopyranoside	*Rhododendron spinuliferum*	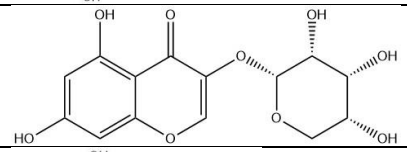	Chromone-143
5-β-D-glucosyloxy-7-hydroxychromone	*Salix matsudana*	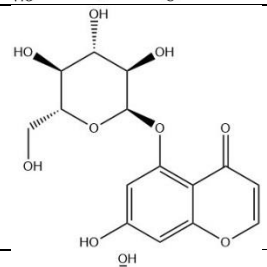	Chromone-144
Schumanniofioside A	*Schumannioph yton magnificum*	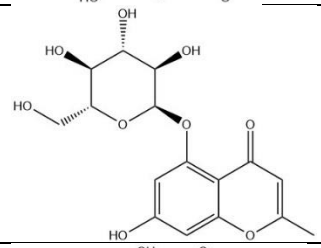	Chromone-145
Schumanniofioside B	*Schumannioph yton magnificum*	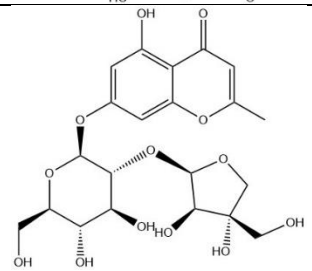	Chromone-146

Name	Plant source	Structure	Name in the manuscript
Rohitukine	*Schumanniophyton magnificum*	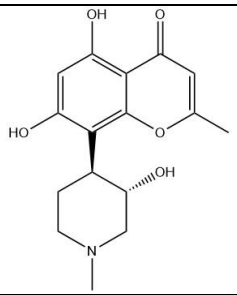	Chromone-147
Schumagnine	*Schumanniophyton magnificum*	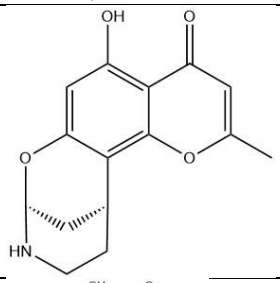	Chromone-148
N-methytschumagnine	*Schumanniophyton magnificum*	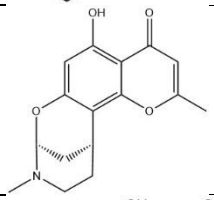	Chromone-149
Sciumanniophytine	*Schumanniophyton magnificum*	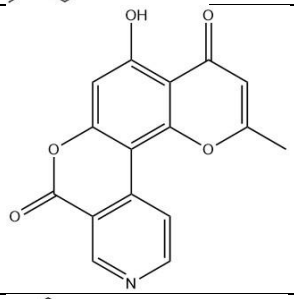	Chromone-150
Isoschumanriiophytine	*Schumanniophyton magnificum*	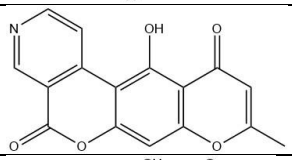	Chromone-151
Uncinoside A	*Selaginella uncinata*	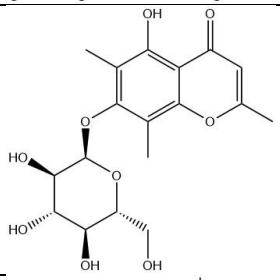	Chromone-152
Uncinoside B	*Selaginella uncinata*	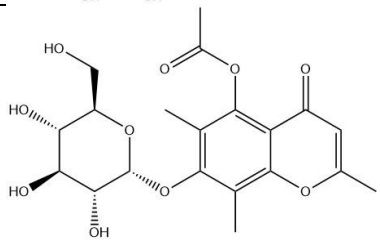	Chromone-153
5-acetonyl-7-hydroxy-2-methylchromone	*Senna siamea*	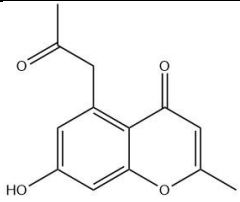	Chromone-154

Name	Plant source	Structure	Name in the manuscript
5-Acetonyl-7-hydroxy-2-hydroxymethylchromone	*Senna siamea*	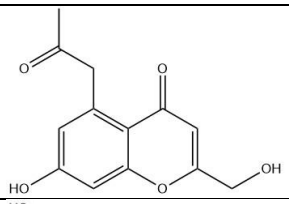	Chromone-155
5-hydroxy-6-(2-Z-butenyl-3-hydroxymethyl)-7-methoxy-2-Methylchromone	*Seseli praecox*	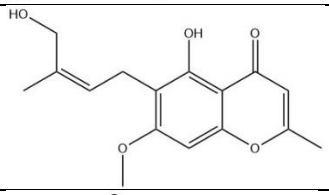	Chromone-156
Seselirin	*Seseli sessiliflorum*	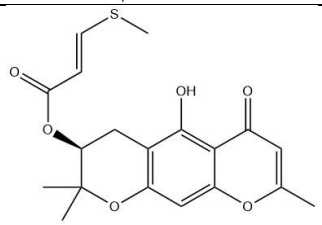	Chromone-157
Sorbifolin	*Spathelia sorbifolia*	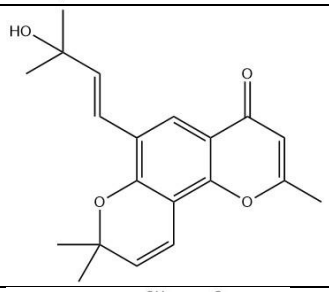	Chromone-158
10-(2', 3'-dihydroxy-3'-methylbutanyl)spatheliachromen	*Spathelia sorbifolia*	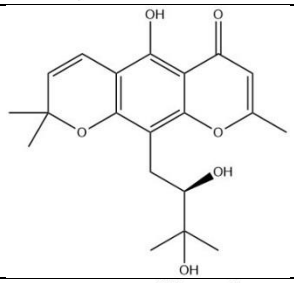	Chromone-159
10-(1', 2', 3'-trihydroxy- 3' -methylbutanyl) spatheliachromen	*Spathelia sorbifolia*	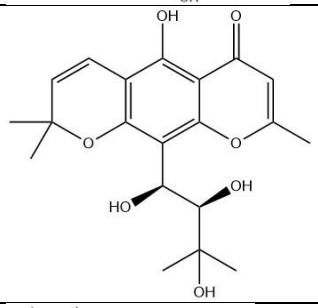	Chromone-160
6-(3'-hydroxy-3'-methyl-*trans*-but-1' -enyl)-O-methylisospatheliachromen	*Spathelia sorbifolia*	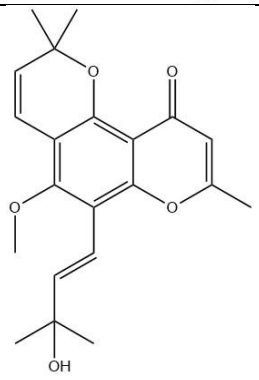	Chromone-161

Name	Plant source	Structure	Name in the manuscript
5-O-methylcneorumchromone K	*Spathelia sorbifolia*	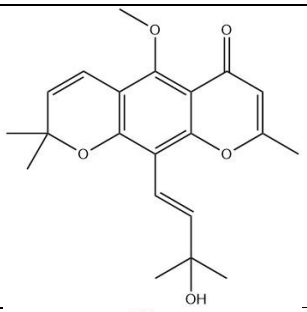	Chromone-162
Isomohsenone	*Stellera chamaejasme*	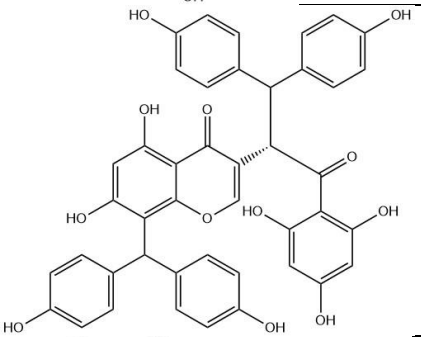	Chromone-163
2-(2-hydroxypentyl)-5-carboxy-7-methoxychromone	*Stratiotes aloides*	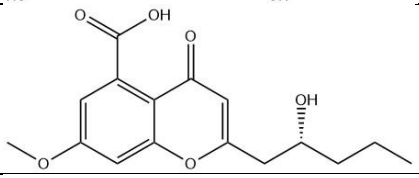	Chromone-164
Terminalianone	*Terminalia brownii*	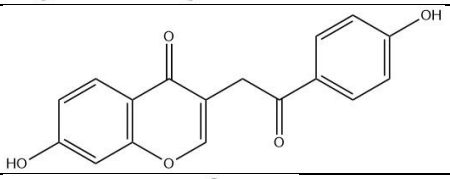	Chromone-165
6-acetyl-7-hydroxy-2,3-dimethyl-chromone	*Tithonia diversifolia*	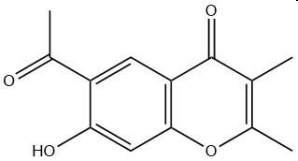	Chromone-166
6-carboxyl-7-Hydroxy-2,3-dimethylchromone	*Tussilago farfara*	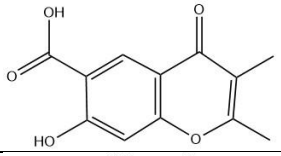	Chromone-167
5-hydroxy-7-methoxy-2-pentylchromone	*Zanthoxylum microcarpum*	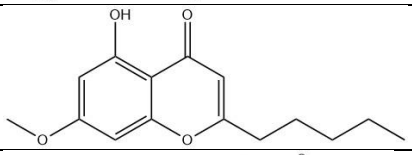	Chromone-168
(E)-2-Acetonyl-8-(2'-O-feruloyl)-β-D-glucopyranosyl-7-methoxy-5-methyl-chromone	*Aloe Africana*	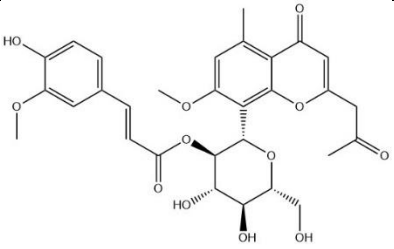	Chromone-169

Name	Plant source	Structure	Name in the manuscript
(E)-2-Acetonyl-(2",6'-di-O,O-coumaroyl)-β-D-glucopyranosyl-7-hydroxy-5-methylchromone	*Aloe Speciosa*	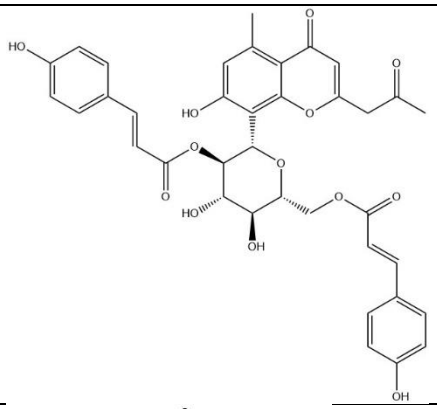	Chromone-170
(E)-2-Acetonyl-8-(2'-O-caffeoyl)-β-D-glucopyranosyl-7-methoxy-5-methyl-chromone	*Aloe Broomii*	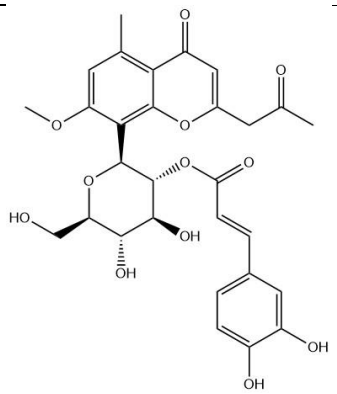	Chromone-171
(E)- 2-Acetonyl-8-[(2'-O-cinnamoyl)-β-D-glucopyranosyl-7-methoxy-5-methylchromone	*Aloe Broomii*	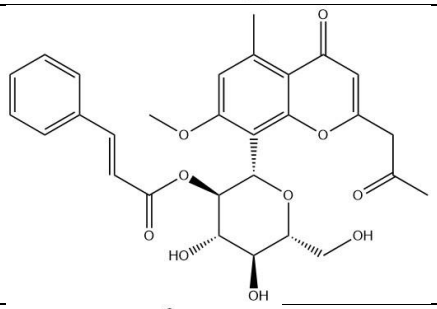	Chromone-172
Aloesin	*Aloe jacksonii*	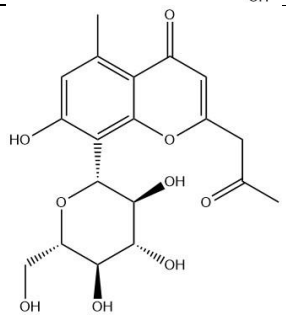	Chromone-173

Grid box parameters

M^{pro} (PDB ID: 6LU7)

center_x = -9.9006, center_y = 11.5016, center_z = 68.4281, size_x = 10.4471, size_y = 20.9610, size_z = 3.5554

Wild type (PDB ID: 6M0J)

center_x = 39.4594, center_y = 55.2385, center_z = 29.5142, size_x = 47.7246, size_y = 17.1081, size_z = 27.2234

Alpha variant (PDB ID: 6MJN)

center_x = 51.2071, center_y = 34.1240, center_z = 59.6830, size_x = 35.4324, size_y = 25.5413, size_z = 32.5547

Beta variant (PDB ID: 7NXA)

center_x = 32.1793, center_y = 38.9480, center_z = 28.8939, size_x = 34.7411, size_y = 28.4815, size_z = 27.2735

Gamma variant (PDB ID: 7NXB)

center_x = 40.8188, center_y = 59.9767, center_z = 43.0356, size_x = 30.1292, size_y = 19.4690, size_z = 36.9062

Delta variant/T478K (PDB ID: 7ORA)

center_x = 31.0654, center_y = 41.3878, center_z = 47.5121, size_x = 22.8610, size_y = 43.1253, size_z = 30.0288

Delta variant/L452R (PDB ID: 7ORB)

center_x = 46.6866, center_y = 52.8883, center_z = 37.6615, size_x = 23.8814, size_y = 35.3059, size_z = 36.3907